iScience

CellPress
OPEN ACCESS

Article

Computational modeling of stem and progenitor cell kinetics identifies plausible hematopoietic lineage hierarchies

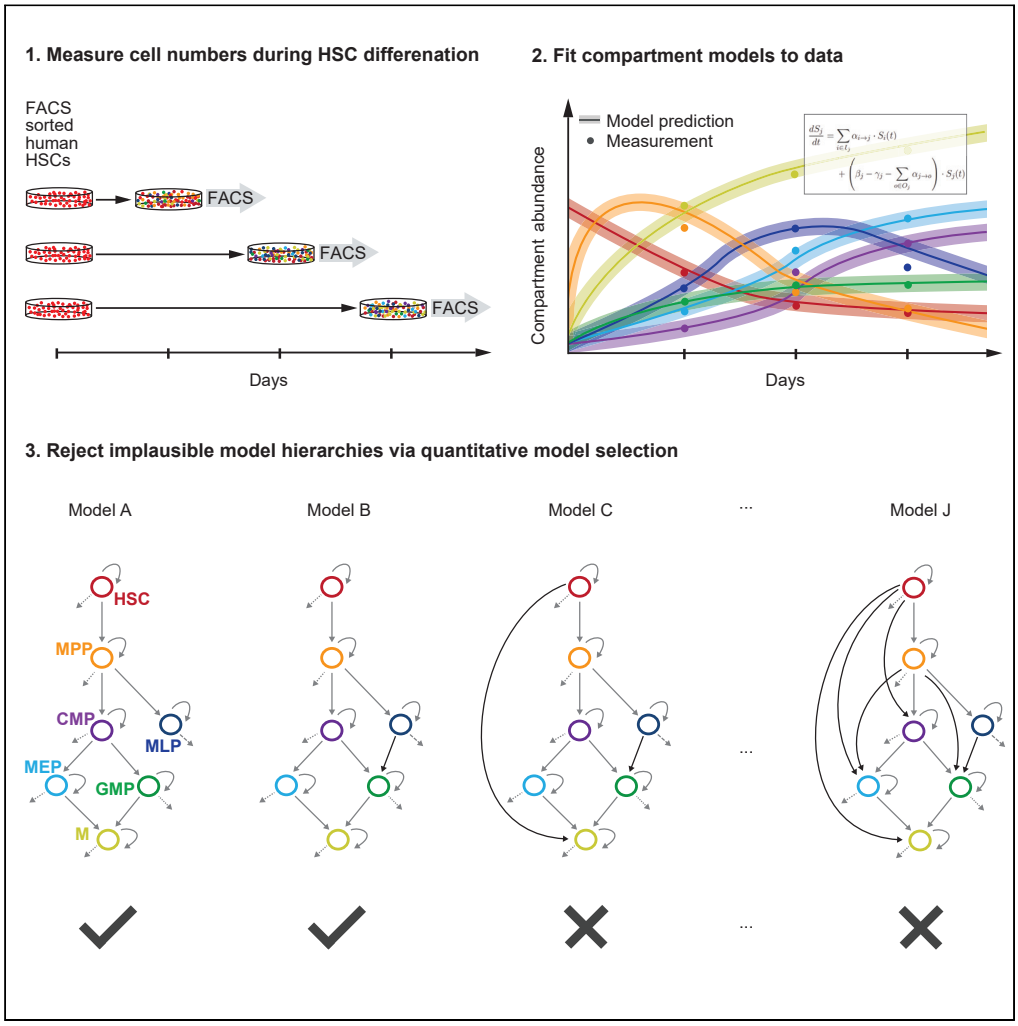

Lisa Bast, Michèle C. Buck, Judith S. Hecker, Robert A.J. Oostendorp, Katharina S. Götze, Carsten Marr

katharina.goetze@tum.de (K.S.G.)
carsten.marr@helmholtz-muenchen.de (C.M.)

HIGHLIGHTS

We assembled 10 lineage hierarchy models of human hematopoiesis

Multiparameter immunophenotyping determines HSC differentiation for 10 healthy donors

ODE fitting and model selection allows to identify plausible hierarchies

A simulation study confirms robustness of model selection for different noise levels

Bast et al., iScience *24*, 102120
February 19, 2021
https://doi.org/10.1016/j.isci.2021.102120

iScience

CellPress
OPEN ACCESS

Article

Computational modeling of stem and progenitor cell kinetics identifies plausible hematopoietic lineage hierarchies

Lisa Bast,[1,2,5,6] Michèle C. Buck,[3,6] Judith S. Hecker,[3] Robert A.J. Oostendorp,[3] Katharina S. Götze,[3,4,*] and Carsten Marr[1,2,7,*]

SUMMARY

Classically, hematopoietic stem cell (HSC) differentiation is assumed to occur via progenitor compartments of decreasing plasticity and increasing maturity in a specific, hierarchical manner. The classical hierarchy has been challenged in the past by alternative differentiation pathways. We abstracted experimental evidence into 10 differentiation hierarchies, each comprising 7 cell type compartments. By fitting ordinary differential equation models with realistic waiting time distributions to time-resolved data of differentiating HSCs from 10 healthy human donors, we identified plausible lineage hierarchies and rejected others. We found that, for most donors, the classical model of hematopoiesis is preferred. Surprisingly, multipotent lymphoid progenitor differentiation into granulocyte-monocyte progenitors is plausible in 90% of samples. An *in silico* analysis confirmed that, even for strong noise, the classical model can be identified robustly. Our computational approach infers differentiation hierarchies in a personalized fashion and can be used to gain insights into kinetic alterations of diseased hematopoiesis.

INTRODUCTION

Identification of the hematopoietic lineage hierarchy is crucial to understand how blood production is controlled and how it is altered in hematopoietic diseases. Current knowledge of human hematopoiesis suggests that the formation of all blood cell types is maintained by a lineage hierarchy, with hematopoietic stem cells (HSCs) at the apex, followed by a set of progenitors that terminate in distinct mature blood cell types. In the classical models of hematopoiesis (Akashi et al., 2000; Doulatov et al., 2012; Manz et al., 2002), HSCs give rise to multipotent progenitors (MPPs), which can differentiate into common myeloid progenitors (CMPs) and multipotent lymphoid progenitors (MLPs). CMPs can further differentiate to megakaryocyte erythrocyte progenitors (MEPs) or granulocyte-monocyte progenitors (GMPs, Figure 1A). Finally, MEPs give rise to erythrocytes and megakaryocytes, which then form platelets, while GMPs differentiate to granulocytes and monocytes. In recent years, this classical model has often been debated as additional or alternative differentiation paths between these cell types have been suggested in humans and mice by a wide range of experimental techniques. Several review studies (Doulatov et al., 2012; Haas et al., 2018; Laurenti and Göttgens, 2018) have summarized these findings and pinpointed the differences in hematopoiesis between mice and humans, but so far, no comprehensive analysis quantitatively assessed the plausibility of competing differentiation hierarchies.

To understand how differentiation paths shape human hematopoiesis, we here assembled and derived 10 competing lineage hierarchies and computationally tested their plausibility. To take advantage of the abundant mouse data and to carefully check all possible transitions rather than to miss any, we decided to include evidence from the murine system. For each lineage hierarchy, we mechanistically modeled cell state kinetics with ordinary differential equations (ODEs) that describe proliferation, differentiation, and cell death for each compartment. In contrast to previous computational approaches, we explicitly accounted for the cell division history and introduced realistic, non-exponential waiting times via intermediate states. To investigate the cell intrinsic differentiation and proliferation potential of human HSCs experimentally, HSCs, 5 different progenitor cell types, and mature cells were defined by cell surface marker expression (Doulatov et al., 2010; Majeti et al., 2007; Manz et al., 2002) and measured by flow cytometry at several time points. The 10 lineage hierarchy models were fitted to the resulting *in vitro* fluorescence

[1]Helmholtz Zentrum München–German Research Center for Environmental Health, Institute of Computational Biology, Neuherberg, Germany

[2]Technical University of Munich, Department of Mathematics, Chair of Mathematical Modeling of Biological Systems, Garching, Germany

[3]Technical University of Munich, School of Medicine, Klinikum rechts der Isar, Department of Internal Medicine III, Munich, Germany

[4]German Cancer Consortium (DKTK), Heidelberg, Partner Site Munich, Germany

[5]Present address: Laboratory of Molecular Neurobiology, Department of Medical Biochemistry and Biophysics, Karolinska Institutet, Solna, Sweden

[6]These authors contributed equally

[7]Lead Contact

*Correspondence: katharina.goetze@tum.de (K.S.G.), carsten.marr@helmholtz-muenchen.de (C.M.)

https://doi.org/10.1016/j.isci.2021.102120

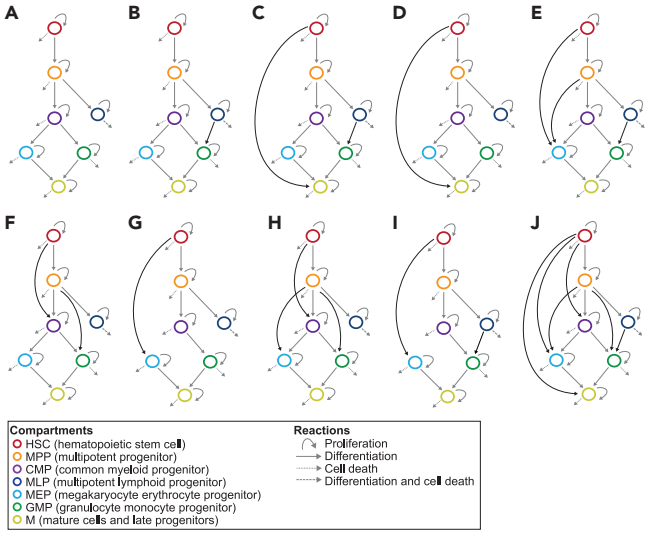

Figure 1. Lineage hierarchies describing healthy hematopoiesis

We constructed 10 different models from hematopoietic hierarchies and differentiation pathways described in the literature (see Methods for a detailed description). Each model consists of a stem cell compartment (HSC), five progenitor compartments (MPPs, MLPs, CMPs, MEPs, GMPs), a compartment comprising late progenitors and mature cells (M). Transitions between states are visualized with arrows, where black arrows indicate transitions that deviate from the classical model (A).

(A) The classical model based on (Akashi et al., 2000) (Akashi et al., 2000; Manz et al., 2002), Laurenti and Göttgens (2018), Haas et al., (2018), and (Doulatov et al., 2012) is the least complex lineage hierarchy with 21 rates.

(B) Same hierarchy as in A but with additional direct differentiation from MLPs to GMPs (22 rates).

(C) Same hierarchy as in B but with additional direct differentiation from HSCs to M compartment (23 rates).

(D) Same hierarchy as in A but with additional direct differentiation from HSCs to Ms (22 rates).

(E) Same hierarchy as in B but with additional direct differentiation from HSCs and MPPs to MEPs (24 rates).

(F) Same hierarchy as in A but with additional direct differentiation from HSCs to CMPs and from MPPs to GMPs (23 rates).

(G) Same hierarchy as in A but replacing the direct differentiation from CMPs to MEPs with the direct differentiation from HSCs to MEPs (21 rates).

(H) Same hierarchy as in A but with additional direct differentiation from HSCs to CMPs, and MPPs to MEPs and GMPs (22 rates).

(I) Same hierarchy as in G but with additional direct differentiation from MLPs to GMPs (22 rates).

(J) Most complex lineage hierarchy incorporating all direct differentiation paths present in any other model (27 rates).

activated cell sorting (FACS) data of differentiating HSCs from 10 healthy donors. Subsequently, we ranked the models' performances according to their Bayesian information criterion (BIC) values to investigate which models can be rejected and which model performs best. An in-depth *in silico* analysis moreover allowed us to identify how accurate our computational approach proves to be, under the assumption of realistic test parameters and for varying noise levels in the data.

RESULTS

Derivation of a set of 10 comparable lineage hierarchies

Our goal was to identify plausible hematopoietic hierarchies by computational modeling. To that end, we compiled hierarchies from previously published experimental studies and review articles of mouse and human hematopoiesis. However, to allow for a systematic evaluation of different proposed hematopoietic hierarchies, we first had to abstract the evidence in these studies to a limited number of cell types and transitions.

The findings from Akashi et al. (2000), Manz et al. (2002), and several review articles (Doulatov et al., 2012; Haas et al., 2018; Laurenti and Göttgens, 2018) provide the basis for the classical hierarchy of human hematopoiesis. Here, HSCs give rise to MPPs, which give rise to CMPs and MLPs. CMPs can further differentiate to MEPs and GMPs, which contribute to mature cells (from now on referred to as the M compartment). This classical hierarchy (Figure 1A) was modified by taking into account reported alternative differentiation

paths. As it has been observed in several studies (Doulatov et al, 2010, 2012; Giebel et al., 2006; Goardon et al., 2011; Reynaud et al., 2003) that MLPs can also differentiate to GMPs, we incorporated the respective transition into 4 hierarchy models (Figures 1B, 1C, 1E, and 1I). Moreover, the existence of a megakaryocyte-primed HSC subset was proposed (Månsson et al., 2007; Sanjuan-Pla et al., 2013), guiding us to include a direct transition from HSCs to the M compartment (Figures 1C and 1D). We furthermore included a direct differentiation transition from MPPs to MEPs, which was observed by Pronk et al. (2007) and Notta et al. (2016) (Figures 1E and 1H). Conflicting observations however have been made regarding the direct transition from HSCs to MEPs (see Adolfsson et al., 2005; Takano et al., 2004 vs. Forsberg et al., 2006), a differentiation transition which we incorporated in three more hierarchies (Figures 1E, 1G, and 1I). Suggested were also the direct differentiation transitions from HSCs to CMPs and from MPPs to GMPs (Adolfsson et al., 2005), which we incorporated in two hierarchies (Figures 1F and 1H). Finally, we considered a hierarchy that comprises all suggested differentiation transitions (Figure 1J). For a detailed description of experimental evidence for differentiation transitions and the derivation of hierarchies, see Transparent methods.

As cells were cultured in media containing specific growth factors at high concentrations (see Transparent methods), we could assume that cells were at any point saturated and not subject to niche effects. We thus did not include any feedback terms in our mathematical models.

Multi-compartment models describe possible cell-intrinsic kinetics

To computationally test the plausibility of the 10 lineage hierarchies (Figure 1) with experimental data, we developed a framework to derive, solve, fit, and rank competing lineage hierarchy models.

The experimental data we used for this analysis were generated by *in vitro* experiments in which HSCs from 10 healthy human bone marrow (BM) samples were stringently sorted as Lineage- CD45dim CD34+ CD38- CD45RA- CD90+ cells, additionally stained with CellTrace division marker, cultured for 7 days in a defined medium optimized for differentiation, and analyzed by multiparameter immunophenotyping on subsequent days (see Transparent methods, Figure S1A and Table S1). This approach allowed us to measure the abundances of 7 cell types for in total 10 samples in a time-resolved manner and track the number of cell divisions between experiment start and the respective observed time point (see Figures S1B and S1C and Transparent methods).

We next derived an ODE compartmental model which considers the 7 cell types as system states and proliferation, differentiation, and cell death events as transitions between these states (Figure 2A shows transitions for the most complex model J) for every candidate hierarchy (Figures 1A–1J). Transitions are defined as reactions that occur with cell-type-specific rates: α for differentiation, β for proliferation, and γ for cell death (Figures 2A and Table 1). While the same proliferation and cell death reactions are considered for each lineage hierarchy model, the set of differentiation reactions is specific for each hierarchy, leading to models with varying complexity (see Transparent methods, Figures 2A and Table 2). For example, model A contains 8 differentiation reactions, 7 proliferation reactions, and 6 cell death reactions (which totals 21 rates), whereas model J contains 14 differentiation reactions and thus a total of 27 rates.

To incorporate the measured cell-type-specific number of divisions since the start of the experiment, we extended this ODE model to include 7 division compartments per cell type. This leads to an increase in state space (from 7 to 49 states), while the parameter space (i.e. the number of unknown rates α, β, γ) stays constant. Every time a cell division occurs, the next division compartment of the same cell type is reached (Figure 2A). When cells change cell type along a differentiation reaction, they stay in the respective division compartment (see Figure 2A inset). Upon arrival at the seventh division compartment (the last one we could reliably measure, see Transparent methods), cells accumulate and can only escape via a differentiation or cell death reaction.

To ensure that differentiation, proliferation, and cell death processes are realistically described by our model, we finally introduced intermediate states for every reaction. Thus, our waiting times are Erlang distributed (Matis and Wehrly, 1990), instead of the conventionally used, unrealistic, exponentially distributed waiting times (Figure 2B). This model extension leads to complex ODE systems with at least 343 and up to 994 equations (see Transparent methods) while again keeping the number of rates constant. The number of intermediate states n_{IS} is a hyperparameter of our model.

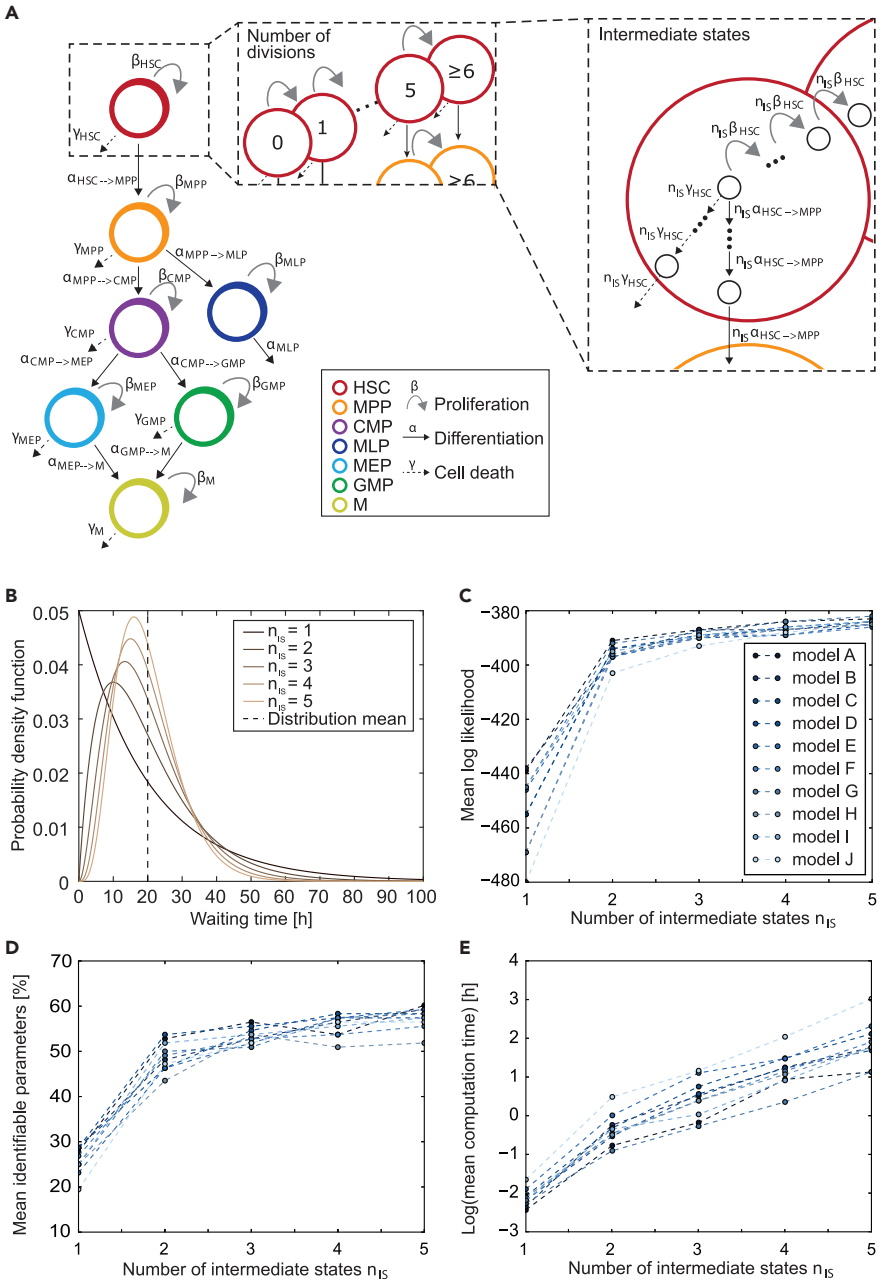

Figure 2. Multi-compartment models with 3 intermediate states show optimal trade-off between parameter inference precision and computational cost

(A) Multi-compartment model accounting for the number of cell divisions and realistic rate distributions via intermediate states (n_{IS}), exemplarily shown for the classical model A. Parameters describe cell-type-specific proliferation, differentiation, and death rates.

(B) Waiting time distributions for 1-5 intermediate states assuming a mean reaction (proliferation, differentiation, or death) rate of 1/20 [h^{-1}].

(C) The mean log likelihood for fitting models A-J (10 lines) to 4 individual samples increases with any additionally introduced intermediate state n_{IS}, especially for introducing a second and third intermediate state.

(D) The mean percentage of practically identifiable parameters sorted by models A-J (10 lines) based on 4 individual samples increases considerably for small n_{IS} but remains roughly constant for $n_{IS} \geq 3$.

(E) The mean computation time for fitting models A-J (10 lines) to the 4 individual samples increases exponentially with the number of intermediate states irrespective of the model hierarchy. For every sample and lineage hierarchy, optimization of 1000 multistarts was run in parallel on 24 workers.

Table 1. All possible state transitions as model reactions in hierarchies A–J

Proliferation reactions	Differentiation reactions		Cell death reactions
R_1 : HSC $\xrightarrow{\beta_{HSC}}$ 2HSC	R_8 : HSC $\xrightarrow{\alpha_{HSC\to MPP}}$ MPP	R_{15} : MPP $\xrightarrow{\alpha_{MPP\to GMP}}$ GMP	R_{22} : HSC $\xrightarrow{\gamma_{HSC}}\varnothing$
R_2 : MPP $\xrightarrow{\beta_{MPP}}$ 2MPP	R_9 : HSC $\xrightarrow{\alpha_{HSC\to CMP}}$ CMP	R_{16} : CMP $\xrightarrow{\alpha_{CMP\to MEP}}$ MEP	R_{23} : MPP $\xrightarrow{\gamma_{MPP}}\varnothing$
R_3 : CMP $\xrightarrow{\beta_{CMP}}$ 2CMP	R_{10} : HSC $\xrightarrow{\alpha_{HSC\to MEP}}$ MEP	R_{17} : CMP $\xrightarrow{\alpha_{CMP\to GMP}}$ GMP	R_{24} : CMP $\xrightarrow{\gamma_{CMP}}\varnothing$
R_4 : MLP $\xrightarrow{\beta_{MLP}}$ 2MLP	R_{11} : HSC $\xrightarrow{\alpha_{HSC\to M}}$ M	R_{18} : MLP $\xrightarrow{\alpha_{MLP\to\cdots}}\varnothing$	R_{25} : MEP $\xrightarrow{\gamma_{MEP}}\varnothing$
R_5 : MEP $\xrightarrow{\beta_{MEP}}$ 2MEP	R_{12} : MPP $\xrightarrow{\alpha_{MPP\to CMP}}$ CMP	R_{19} : MLP $\xrightarrow{\alpha_{MLP\to GMP}}$ GMP	R_{26} : GMP $\xrightarrow{\gamma_{GMP}}\varnothing$
R_6 : GMP $\xrightarrow{\beta_{GMP}}$ 2GMP	R_{13} : MPP $\xrightarrow{\alpha_{MPP\to MLP}}$ MLP	R_{20} : MEP $\xrightarrow{\alpha_{MEP\to M}}$ M	R_{27} : M $\xrightarrow{\gamma_{M}}\varnothing$
R_7 : M $\xrightarrow{\beta_{M}}$ 2M	R_{14} : MPP $\xrightarrow{\alpha_{MPP\to MEP}}$ MEP	R_{21} : GMP $\xrightarrow{\alpha_{GMP\to M}}$ M	

HSC, MPP, CMP, MLP, MEP, GMP, and M indicate cell types (see Figure 1), $\varnothing$ denotes the empty set, and $r \in \{\alpha_{(.)}, \beta_{(.)}, \gamma_{(.)}\}$ the reaction rates (see Figure 2).

Before fitting to experimental data, we analyzed structural identifiability of the 10 competing models with the MATLAB toolbox STRIKE-GOLDD (Villaverde et al., 2019; Villaverde and Banga, 2017). Under the assumption of ideal, noise-free experimental data, all proliferation, differentiation, and cell death rates can be inferred from the measurements. This holds independently of the chosen model hierarchy and independently of considering proliferation count compartments if three intermediate states are assumed. Interestingly, for models C, D, E, and J, some rates are not structurally identifiable if proliferation count compartments but no intermediate states are considered and most parameters especially proliferation and death rates are unidentifiable if no proliferation counts and no intermediate states are considered (Table 3).

Parameter inference identifies optimal number of intermediate states

We implemented all 10 models for an arbitrary number of intermediate states n_{IS} in MATLAB and used the AMICI toolbox (Fröhlich et al., 2017) to determine the solution of the ODE system. Solving the ODE system is required to simulate observations from the models for certain parameter combinations while maximizing the likelihood function. As we observed and modeled cell counts, we assumed log normally distributed noise in the likelihood function. We applied a hierarchical optimization approach (Loos et al., 2018) with which the division compartment and cell type compartment-specific noise parameters are analytically calculated during optimization. Using the profile likelihood method (Kreutz et al., 2013), we calculated the 95% confidence interval for each parameter, each model, and each donor sample. Next, we optimized the number of intermediate states n_{IS} that are required to accurately and efficiently estimate and practically identify model parameters. Specifically, we fitted all 10 models with 1–5 intermediate states (in total 50 models) to 4 randomly chosen samples. We observed that for all models A-J, the log likelihood increases with the number of intermediate states n_{IS} (Figure 2C). However, the mean percentage increase in log likelihood per additional intermediate state is below 3% for $n_{IS} > 3$. As the percentage of practically identifiable parameters plateaus at $n_{IS} = 3$ (see Transparent methods), we fixed this hyperparameter and performed the remaining analysis with $n_{IS} = 3$ intermediate states.

We fitted every model A-J with 3 intermediate states to all 10 samples (see Figure 3A for the fit of model A to one exemplary donor sample) using maximum likelihood estimation (see Transparent methods) and multistart optimization with the MATLAB toolbox PESTO (Stapor et al., 2018). As indicated by narrow confidence intervals for almost all samples (Figure 3B), we observed that most rates could be inferred from the data with high certainty (Table S3 lists all $\log_{10}$ transformed parameter values with their confidence intervals for model A). We thus concluded that overall, practical identifiability of parameters is given. However, identifiability deteriorates for the downstream progenitor compartments (GMP and MEP), especially for differentiation and cell death rates, for which we observe larger confidence intervals compared to upstream compartments (Figure 3B) and practical identifiability is not always guaranteed. Practical non-identifiability of a parameter is indicated by confidence intervals that include the upper or lower border or both borders of the parameter's search space (e.g. γ_{MEP} for sample 1 in Figure 3B).

Model comparison reveals plausible lineage hierarchies

To determine which lineage hierarchies best explained our experimental data, we performed quantitative model selection. This was done by assigning a score to each of the 10 models and every individual sample. We calculated the BIC (Schwartz, 1965), which takes goodness of fit, number of parameters, and the number of data points

Table 2. Model complexity indicated by the number of reaction rates for lineage hierarchies A–J

Model	# Reaction rates	Reactions
A	21	$R_1 - R_8, R_{12} - R_{13}, R_{16} - R_{18}, R_{20} - R_{27}$
B	22	$R_1 - R_8, R_{12} - R_{13}, R_{16} - R_{27}$
C	23	$R_1 - R_8, R_{11} - R_{13}, R_{16} - R_{27}$
D	22	$R_1 - R_8, R_{11} - R_{13}, R_{16} - R_{18}, R_{20} - R_{27}$
E	24	$R_1 - R_8, R_{10}, R_{12} - R_{14}, R_{16} - R_{27}$
F	23	$R_1 - R_9, R_{13}, R_{16} - R_{18}, R_{20} - R_{27}$
G	21	$R_1 - R_8, R_{10}, R_{12} - R_{13}, R_{17}, R_{18}, R_{20} - R_{27}$
H	22	$R_1 - R_9, R_{13} - R_{14}, R_{16} - R_{18}, R_{20} - R_{27}$
I	22	$R_1 - R_8, R_{10}, R_{12} - R_{13}, R_{17} - R_{27}$
J	27	$R_1 - R_{27}$

The corresponding reactions are listed in Table 1.

into account (see Transparent methods). After calculating model- and sample-specific BIC scores, we ranked the models accordingly and assessed how often a respective model was the best performing one (lowest score among the considered models), among the plausible models (BIC difference in score to best model <10), or how often it was rejected (BIC difference to best model $\geq$10, see Figures 3C and 3D).

Based on our analysis, there is no evidence in our data for models E, H, and J, which were rejected for all donor samples according to BIC. Models C, F, and I also performed poorly, as they were rejected for more than 80% of samples. The only model which was not rejected by a single sample is the classical lineage hierarchy A. It was selected as the best performing model in 90% of the samples based on BIC. Model B was considered as plausible for almost 90% of the samples according to BIC (Figure 3D). There is also some evidence for models D and G, which are plausible for 30% of the samples.

To investigate if the outstanding performance of model A mainly stems from its low complexity, we additionally calculated the Akaike information criterion (AIC, Akaike, 1992). As this selection criterion penalizes the number of parameters in the model differently than BIC, it can potentially select and reject other models. Indeed, the AIC is less conservative than the BIC for the model complexities of interest and the range of the number of data points we used for the fit (Figure S2A). For AIC, we again found support for models A and B, whereas models E, F, H, I, and J performed as poorly as in the BIC ranking (Figures 3D and S2B). According to AIC, there is more evidence for model C (rejected in only 60% of samples as

Table 3. Structurally unidentifiable parameters for models A–J with and without 3 intermediate states and 7 proliferation count compartments

	Unidentifiable parameters			
Model	$n_{IS} = 1, n_{div} = 7$	$n_{IS} = 3, n_{div} = 7$	$n_{IS} = 1, n_{div} = 1$	$n_{IS} = 3, n_{div} = 1$
A	$x_0(\theta)$	$x_0(\theta)$	$x_0(\theta), \beta_\cdot, \alpha_{MLP\rightarrow\ldots}, \gamma_\cdot$	$x_0(\theta)$
B	$x_0(\theta)$	$x_0(\theta)$	$x_0(\theta), \beta_\cdot, \alpha_{MLP\rightarrow\ldots}, \gamma_\cdot$	$x_0(\theta)$
C	$x_0(\theta), \alpha_{GMP\rightarrow M}, \gamma_{GMP}$	$x_0(\theta)$	$x_0(\theta), \beta_\cdot, \alpha_{MLP\rightarrow\ldots}, \alpha_{GMP\rightarrow M}, \gamma_\cdot$	$x_0(\theta)$
D	$x_0(\theta), \alpha_{GMP\rightarrow M}, \gamma_{GMP}$	$x_0(\theta)$	$x_0(\theta), \beta. \alpha_{MLP\rightarrow\ldots}, \alpha_{GMP\rightarrow M}, \gamma_\cdot$	$x_0(\theta)$
E	$x_0(\theta), \alpha_{CMP\rightarrow MEP}, \gamma_{CMP}$	$x_0(\theta)$	$x_0(\theta), \beta_\cdot, \alpha_{MLP\rightarrow\ldots}, \alpha_{CMP\rightarrow MEP}, \gamma_\cdot$	$x_0(\theta)$
F	$x_0(\theta)$	$x_0(\theta)$	$x_0(\theta), \beta_\cdot, \alpha_{MLP\rightarrow\ldots}, \gamma_\cdot$	$x_0(\theta)$
G	$x_0(\theta)$	$x_0(\theta)$	$x_0(\theta), \beta_\cdot, \alpha_{MLP\rightarrow\ldots}, \gamma_\cdot$	$x_0(\theta)$
H	$x_0(\theta)$	$x_0(\theta)$	$x_0(\theta), \beta_\cdot, \alpha_{MLP\rightarrow\ldots}, \gamma_\cdot$	$x_0(\theta)$
I	$x_0(\theta)$	$x_0(\theta)$	$x_0(\theta), \beta_\cdot, \alpha_{MLP\rightarrow\ldots}, \gamma_\cdot$	$x_0(\theta)$
J	$\alpha_{MLP\rightarrow GMP}, \alpha_{MLP}, x_0(\theta)$	$x_0(\theta)$	$x_0(\theta), \beta_\cdot, \alpha_{MLP\rightarrow\ldots}, \alpha_{MLP\rightarrow MEP}, \alpha_{GMP\rightarrow M}, \gamma_\cdot$	$x_0(\theta)$

$x_0(\theta)$ is the set of parameters describing the initial conditions of the respective ordinary differential equation (ODE) system (see Transparent methods).

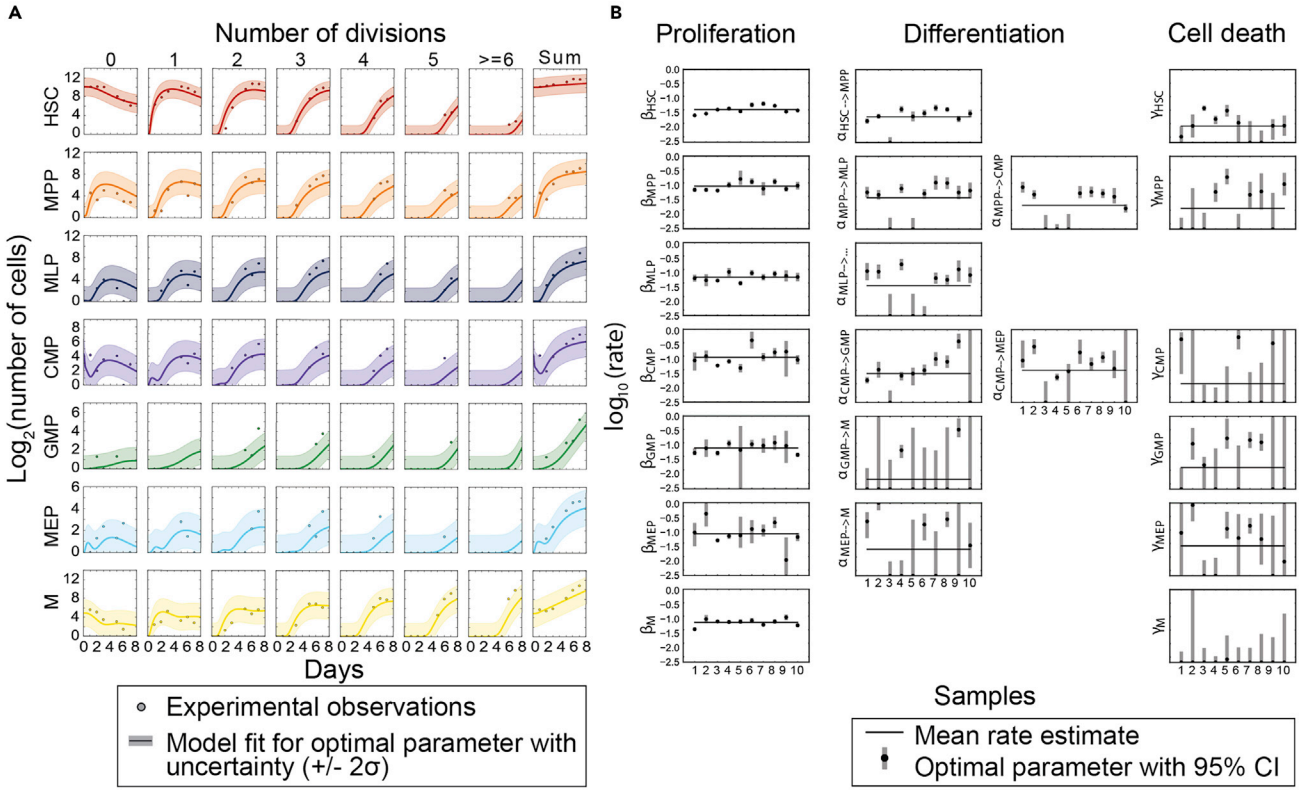

C

Model \ Sample	1	2	3	4	5	6	7	8	9	10
A	1550	881	721	795	370	632	1157	1060	822	938
B	1559	889	729	795	376	641	1164	1073	824	943
C	1570	889	752	815	389	655	1174	1092	828	952
D	1559	882	744	808	382	642	1169	1075	825	950
E	1578	900	761	838	394	660	1183	1107	833	960
F	1587	929	759	808	377	677	1214	1156	832	947
G	1569	897	762	817	378	661	1180	1120	819	939
H	1590	919	765	822	384	669	1210	1143	835	955
I	1580	903	745	826	384	667	1190	1131	820	948
J	1609	918	843	867	416	683	1221	1143	850	984

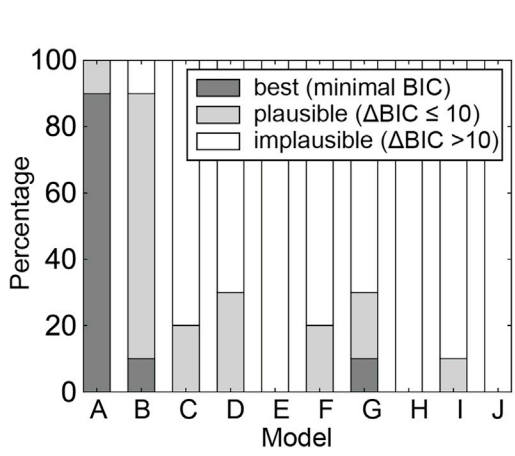

Figure 3. Quantitative model comparison reveals model A as the most plausible lineage hierarchy (see also Figure S2)

(A) Model A (solid line) was fitted to cell abundances in 49 compartments observed for sample 1 (dots). Model uncertainty is shown as ± 2σ error bands. Sum over all divisions for each cell type compartment (last column) was not used for the fit but shows agreement of model fit and data.

(B) Optimal parameter values (dots) with 95% confidence intervals (boxes) result from fitting model A to all 10 samples.

(C) Bayesian information criterion (BIC) values per model A-J (rows) for every individual sample (columns) result from fitting all considered lineage hierarchies (Figures 1A–1J) to samples of 10 healthy individuals. Color code corresponds to three categories, which were defined based on BIC scoring. Models were categorized into best (for the lowest score), plausible (a difference to the lowest BIC score ≤10), and implausible (a difference to the lowest score >10) models for each donor sample.

(D) Relative frequency of a model to belong to one of the three categories best, plausible, and implausible according to the BIC scores obtained from the 10 samples.

compared to 80% with BIC) and model D (rejected with BIC in only 40% of samples as compared to 70%) but not for model G (rejected in 70% of the samples for both criteria). With a rejection percentage of at least 70% of samples according to both criteria (AIC and BIC), models E-J can be overall rejected.

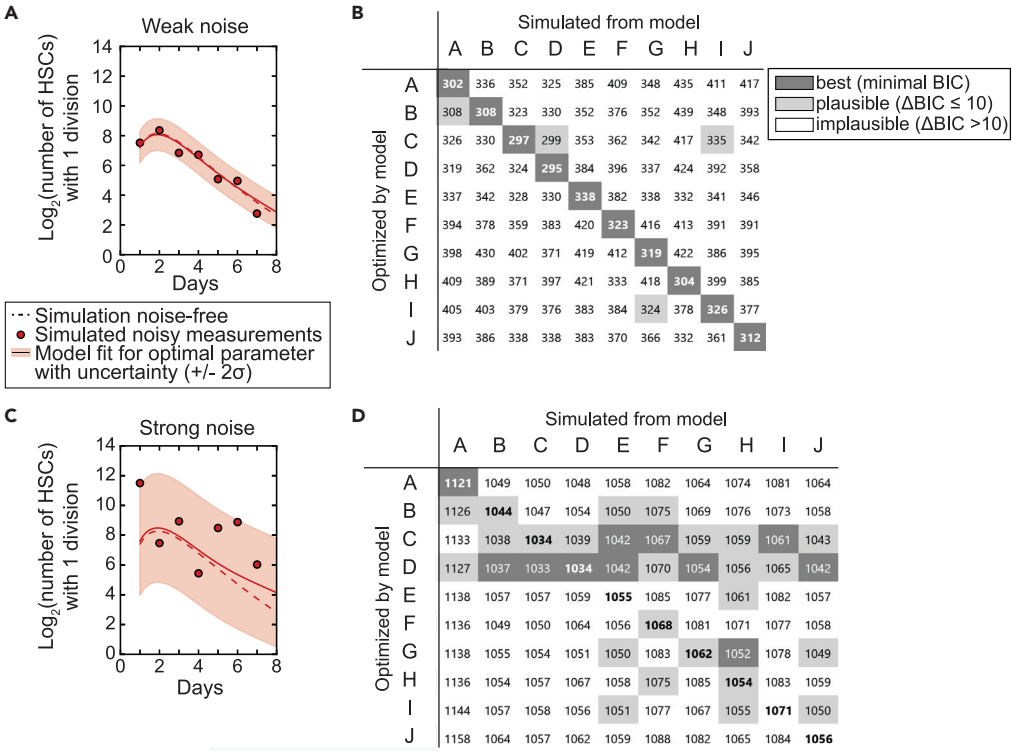

Figure 4. Lineage hierarchy identification is robust for varying noise levels (see also Figure S3)

(A) Weak noise simulation and fit of model A, exemplarily shown for HSCs that have divided once. Simulated data (dashed line) were perturbed with weak noise (σ = 0.4, dots). The true kinetics (dashed line) deviates only slightly from the fitted model (solid line) and is contained in the $\pm$ 2σ error band depicting model uncertainty.

(B) For weak noise, the best fitting model always coincides with the simulated ground truth. Data was simulated with a realistic test parameter set for each model A-J and perturbed with weak noise (σ = 0.4, as shown in A). BIC values result from fitting simulated data with models A-J. The lowest BIC value (dark gray boxes) appears always for the true model and only up to two other models are plausible (light gray boxes).

(C) Strong noise simulation and fit of model A, exemplarily shown for HSCs that have divided once. Simulated data (dashed line) was perturbed with strong noise (σ = 1.2, dots). The true kinetics (dashed line) deviates at later time points from the fitted model (solid line) but is contained in the $\pm$ 2σ error band depicting model uncertainty.

(D) For strong noise (σ = 1.2, as shown in C), only models A and D are correctly identified as the best performing model (dark gray boxes on diagonal). For data simulated from models B, C, F, G, and H the true lineage hierarchy is not the best performing model but considered as plausible (light gray boxes on diagonal). For data simulated from models E and J, the true model was assessed as implausible (white boxes on diagonal) based on the BIC value.

Robust identification of lineage hierarchies

To investigate if it is in principle possible to select the true underlying model and not necessarily the least complex one, we performed an *in silico* model selection analysis. For this purpose, we chose a realistic model-specific parameter set, which was equal to the mean rate estimates from the experimental data (shown for model A in Figure 3B). We subsequently simulated artificial data from every model A-J, perturbed the generated data with noise of varying strengths (see Figure S3A for an exemplary simulation), and fitted the perturbed artificial samples with every model A-J (see Figure S3B for corresponding true and inferred parameter values). For weak noise, the measurement points deviated only lightly from the simulated values (noise parameter σ = 0.4, Figure 4A), whereas for strong noise, the perturbed measurements scattered strongly (noise parameter σ = 1.2, Figure 4C). Interestingly, for every *in silico* sample generated with weak noise, the true model (that is, the model from which the data were generated) performed best and almost all (8 or 9 out of 9 other models) were rejected (Figure 4B). For strong noise, we found that the true model was only accurately identified for lineage hierarchies A and D (Figure 4D). Model D is however also at least plausible if the data were simulated from any other model (Figure 4D). For model I and the two most complex models E and J, other models were favored and the true model was rejected (Figure 4D). This analysis shows how crucial underlying noise is for the robust identification of the true model. However

even for strong noise, model A was never the best performing model when the *in silico* data was generated from another lineage hierarchy and not even considered as plausible, suggesting its low complexity is not the predominant feature of its outstanding performance (Figures 4B and 4D). For models E and J on the contrary, the model complexity might have been a barrier in correctly identifying them in the presence of strong noise: Model E was identified only once as a plausible model, model J never (Figure 4D). While simulating from model I, model C was selected as the best model, despite its higher complexity (23 vs. 22 parameters), while model I itself was rejected. Interestingly, the noise parameters per cell type and division compartment that were estimated from the experimental data (Figure 3) all lie in the interval [0.6,1.1] and are thus stronger than the weak noise ($\sigma = 0.4$) but also weaker than the strong noise ($\sigma = 1.2$) which were assumed in the *in silico* analysis.

Based on this analysis, we can conclude that our parameter inference approach allows for the robust identification of lineage hierarchies in the presence of noise, if it is not overprominent. Most importantly, it is unlikely that model A was only selected due to its low complexity.

DISCUSSION

Although many aspects of the hematopoietic system are well characterized after decades of research, substantial gaps in our understanding of how the different blood cell types are produced remain, in particular when it comes to human hematopoiesis, where evidence and access is substantially scarcer than in mice. We approached this gap by quantitatively comparing 10 lineage hierarchies, integrating the evidence from a broad range of experimental studies. We found that our data supported the classical model of hematopoiesis, that an additional differentiation transition from MLPs to GMPs is plausible, but no evidence to support the validity of the remaining 8 lineage hierarchies.

Our approach is based on 7 distinctly defined human hematopoietic cell types. This is complementary to a recently reported combined index-FACS and single-cell transcriptomic analysis (Velten et al., 2017). By projecting transcriptomic similarity of single hematopoietic cells on a unit circle, Velten et al. (2017) could observe a "Continuum of LOw primed UnDifferentiated hematopoietic stem- and progenitor cells (CLOUD-HSPCs)". Interestingly, our finding that the additional transition from MLPs to GMPs (Figure 1B) is plausible in 90% of the samples (Figure 3D) is in line with their finding that a small subpopulation of MLPs in the two samples they analyzed differentiate toward neutrophils (Fig. 5b and Supplemental Fig. 5b in Velten et al. (2017)). It also fits with the recently reported joint progenitor population of B cells and plasmacytoid dendritic cells in mice (Herman et al., 2018). While our approach cannot resolve continuous transitions by design, it facilitates the direct inference of differentiation, proliferation, and cell death rates. Thereby, we circumvent that inferred differentiation rates are often biased by cell cycle effects, which is currently a challenge in differentiation trajectory inference from scRNAseq data (Watcham et al., 2019; Weinreb et al., 2018).

Hematopoiesis as a paradigmatic stem cell system has been described in the past with a few data-driven models. In Busch et al. (2015), mouse *in vivo* lineage tracing data were used to parametrize a computational ODE-based compartment model of HSCs, MPPs, CLPs, and CMPs. Parameter inference revealed cell type-specific differentiation and net proliferation rates based on the upper part of the classical hierarchy since only late progenitors (GMPs and MEPs) but not mature cells were measured in the experiment. A model by Klose et al. (2019) included internal feedback within a heterogeneous HSC population and is suited to consistently describe both hematopoietic homeostasis and regeneration upon injury. It was validated using the experimental mouse data from Busch et al. (2015) but only considered one progenitor compartment without distinguishing between the various progenitor cell types. They model heterogeneity in the HSC compartment by considering two HSC subtypes: repopulating HSCs which are rarely activated during homeostasis, and maintaining HSCs which ensure the continuous supply of progenitor cells. Assuming steady-state hematopoiesis their analysis showed that repopulating HSCs differentiate and proliferate at a much lower rate than maintaining HSCs and progenitors, which differentiate almost as fast as they proliferate. In contrast to these approaches, we modeled cellular rates with realistic, Erlang distributed waiting time, leading to an improved fitting of the model to the data. Similar to our *in vitro* experiments, time-resolved cell counts from mouse *in vitro* lineage negative, Sca1 positive, c-kit negative (LSK) cell cultures (comprising long-term (LT) HSCs, short-term (ST) HSCs, and MPPs) were used previously (Adimy and Crauste, 2009; Busch et al., 2015; Klose et al., 2019; Mahadik et al., 2019) for model fitting. In particular the influence of different culture conditions on the balance between HSC self-renewal vs. differentiation and

proliferation was studied by considering 3 (LSK, CMP, terminal) and 5 (LT HSC, ST HSC, MPP, CMP, terminal) compartment ODE models. Interestingly, feedback and some recently suggested differentiation transitions (LSK to terminal, and ST HSC and MPP to terminal, respectively) were included in the model. The authors conclude that downstream differentiation is driven by rapid differentiation of ST repopulating HSC progenitor populations and not CMPs and thereby favor the additionally included differentiation transitions. In contrast to our approach, the plausibility of the suggested 3- or 5-compartment models was neither assessed nor quantitatively compared and cell divisions were neither tracked nor modeled.

We modeled hematopoiesis deterministically with ODEs since hundreds to thousands of cells were observed in our *in vitro* culture and stochastic effects average out. Per design of our cell culture experiment, extrinsic niche effects were not considered and cells were not competing for space or growth factors. Consequently, we modeled unlimited cell population growth without any feedback. To apply our approach to *in vivo* data or to cell cultures with only few cells and limited space or growth factors, the model would need to be adapted to e.g. include feedback terms and a carrying capacity (Klose et al., 2019; MacLean et al., 2014), use a stochastic formalism (Marr et al., 2012; Newton et al., 1995; Strasser et al., 2018; Xu et al., 2018), or incorporate space or cell age via partial differential equations (Craig et al., 2016; Østby et al., 2003; Roeder et al., 2009).

Detailed insights into differentiation pathways and rates are critical for understanding how hematopoiesis yields sufficient blood cells throughout the lifetime of an individual. Improving our understanding of cell-type-specific differentiation, proliferation, and cell death may help to predict how hematologic diseases develop and how they respond to therapy. Our computational approach provides access to these parameters and may facilitate comparisons of benign and leukemic kinetics to healthy hematopoiesis to identify cell types and rates affected in leukemogenesis. It might thus also help to uncover targetable cell intrinsic disease mechanisms in the future.

Limitations of the study

In theory, differentiation transitions may exist which we have not tested, or transitions may exist that our present approach could not identify. The latter could be due to relatively high noise in the count data in combination with a very low differentiation rate of the respective transition. Also, it is worth mentioning that we focussed only on cell intrinsic kinetics—constraints of the BM environment that affect the differentiation hierarchy are not considered in our *in vitro* setting. Similarly, our model would need to be changed if one aims to describe cell cultures in which cells are competing for space or growth factors.

The experimental setup and used technology limits the number of cell types which could be determined by flow cytometry. By using additional markers and expanding the model, additional hypotheses regarding the differentiation paths, i.e., involving specific mature cell types could be tested.

Resource availability

Lead contact

Requests for resources and reagents should be directed to the lead contact Carsten Marr (carsten.marr@helmholtz-muenchen.de).

Material availability

This study did not generate new unique reagents.

Data and code availability

Cell counts for the measured division and cell type compartments and easily executable, documented code in MATLAB and Python are publicly accessible at https://github.com/marrlab/HematopoiesisModelComparison.

METHODS

All methods can be found in the accompanying Transparent methods supplemental file.

SUPPLEMENTAL INFORMATION

Supplemental information can be found online at https://doi.org/10.1016/j.isci.2021.102120.

ACKNOWLEDGMENTS

We would like to thank Hans Knabe for providing healthy bone marrow samples. Moreover, we thank Ali Boushehri for reviewing MATLAB and Python code of our analysis and Melanie Schulz and Lea Schuh for feedback on the manuscript. This work was supported by research grants from the Deutsche Forschungsgemeinschaft, SFB 1243 for projects A09 (M.B., K.S.G., R.A.J.O.), A17 (L.B., C.M.), and FOR2033 project B3 (K.S.G. and R.A.J.O.), as well as the Deutsche Jose Carreras Leukämie Stiftung (DJCLS, R14/18, K.S.G.). L.B. further acknowledges financial support by the Joachim Herz Stiftung. C.M. has received funding from the European Research Council (ERC) under the European Union's Horizon 2020 research and innovation program (Grant agreement No. 866411). K.S.G has received funding from the European Research Council under the Eurpoean Unions's Horizon 2020 Marie Sklodowska-Curie programme (Grant agreement No. 953407).

AUTHOR CONTRIBUTIONS

L.B. derived the set of lineage hierarchies and mathematical models, implemented and performed parameter inference, model selection and *in silico* analysis, analyzed results, and drafted the manuscript. M.C.B. designed, established, and performed *in vitro* experiments, derived the set of lineage hierarchies, and drafted the manuscript. J.S.H. collected BM samples and donor data. R.A.J., K.S.G., and C.M. designed experiments, analyzed results, and wrote the manuscript. All authors read and agreed with the final version of the manuscript.

DECLARATION OF INTERESTS

The authors declare no competing interests.

Received: November 6, 2020
Revised: January 8, 2021
Accepted: January 22, 2021
Published: February 19, 2021

REFERENCES

Adimy, M., and Crauste, F. (2009). Mathematical model of hematopoiesis dynamics with growth factor-dependent apoptosis and proliferation regulations. Math. Comput. Model. https://doi.org/10.1016/j.mcm.2008.07.014.

Adolfsson, J., Månsson, R., Buza-Vidas, N., Hultquist, A., Liuba, K., Jensen, C.T., Bryder, D., Yang, L., Borge, O.-J., Thoren, L.A.M., et al. (2005). Identification of Flt3+ lympho-myeloid stem cells lacking erythro-megakaryocytic potential a revised road map for adult blood lineage commitment. Cell *121*, 295–306.

Akaike, H. (1992). Information Theory and an Extension of the Maximum Likelihood Principle (Springer Series in Statistics). https://doi.org/10.1007/978-1-4612-0919-5_38.

Akashi, K., Traver, D., Miyamoto, T., and Weissman, I.L. (2000). A clonogenic common myeloid progenitor that gives rise to all myeloid lineages. Nature *404*, 193–197.

Busch, K., Klapproth, K., Barile, M., Flossdorf, M., Holland-Letz, T., Schlenner, S.M., Reth, M., Höfer, T., and Rodewald, H.-R. (2015). Fundamental properties of unperturbed haematopoiesis from stem cells in vivo. Nature *518*, 542–546.

Craig, M., Humphries, A.R., and Mackey, M.C. (2016). A mathematical model of granulopoiesis incorporating the negative feedback dynamics and kinetics of G-CSF/neutrophil binding and internalization. Bull. Math. Biol. *78*, 2304–2357.

Doulatov, S., Notta, F., Eppert, K., Nguyen, L.T., Ohashi, P.S., and Dick, J.E. (2010). Revised map of the human progenitor hierarchy shows the origin of macrophages and dendritic cells in early lymphoid development. Nat. Immunol. *11*, 585–593.

Doulatov, S., Notta, F., Laurenti, E., and Dick, J.E. (2012). Hematopoiesis: a human perspective. Cell Stem Cell *10*, 120–136.

Forsberg, E.C., Serwold, T., Kogan, S., Weissman, I.L., and Passegué, E. (2006). New evidence supporting megakaryocyte-erythrocyte potential of flk2/flt3+ multipotent hematopoietic progenitors. Cell *126*, 415–426.

Fröhlich, F., Kaltenbacher, B., Theis, F.J., and Hasenauer, J. (2017). Scalable parameter estimation for genome-scale biochemical reaction networks. PLoS Comput. Biol. *13*, e1005331.

Giebel, S., Wojnar, J., Krawczyk-Kulis, M., Markiewicz, M., Wylezoł, I., Seweryn, M., Holowiecka-Goral, A., and Holowiecki, J. (2006). Treosulfan, cyclophosphamide and antithymocyte globulin for allogeneic hematopoietic cell transplantation in acquired severe aplastic anemia. Ann. Transpl. *11*, 23–27, discussion 32–43.

Goardon, N., Marchi, E., Atzberger, A., Quek, L., Schuh, A., Soneji, S., Woll, P., Mead, A., Alford, K.A., Rout, R., et al. (2011). Coexistence of LMPP-like and GMP-like leukemia stem cells in acute myeloid leukemia. Cancer Cell *19*, 138–152.

Haas, S., Trumpp, A., and Milsom, M.D. (2018). Causes and consequences of hematopoietic stem cell heterogeneity. Cell Stem Cell *22*, 627–638.

Herman, J.S., Sagar, and Grün, D. (2018). FateID infers cell fate bias in multipotent progenitors from single-cell RNA-seq data. Nat. Methods *15*, 379–386.

Klose, M., Florian, M.C., Gerbaulet, A., Geiger, H., and Glauche, I. (2019). Hematopoietic stem cell dynamics are regulated by progenitor demand: lessons from a quantitative modeling approach. Stem Cells *37*, 948–957.

Kreutz, C., Raue, A., Kaschek, D., and Timmer, J. (2013). Profile likelihood in systems biology. FEBS J. *280*, 2564–2571.

Laurenti, E., and Göttgens, B. (2018). From haematopoietic stem cells to complex differentiation landscapes. Nature *553*, 418–426.

Loos, C., Krause, S., and Hasenauer, J. (2018). Hierarchical optimization for the efficient parametrization of ODE models. Bioinformatics *34*, 4266–4273.

MacLean, A.L., Filippi, S., and Stumpf, M.P.H. (2014). The ecology in the hematopoietic stem cell niche determines the clinical outcome in chronic myeloid leukemia. Proc. Natl. Acad. Sci. U S A *111*, 3883–3888.

Mahadik, B., Hannon, B., and Harley, B.A.C. (2019). A computational model of feedback-mediated hematopoietic stem cell differentiation in vitro. PLoS One *14*, e0212502.

Majeti, R., Park, C.Y., and Weissman, I.L. (2007). Identification of a hierarchy of multipotent hematopoietic progenitors in human cord blood. Cell Stem Cell *1*, 635–645.

Månsson, R., Hultquist, A., Luc, S., Yang, L., Anderson, K., Kharazi, S., Al-Hashmi, S., Liuba, K., Thorén, L., Adolfsson, J., et al. (2007). Molecular evidence for hierarchical transcriptional lineage priming in fetal and adult stem cells and multipotent progenitors. Immunity *26*, 407–419.

Manz, M.G., Miyamoto, T., Akashi, K., and Weissman, I.L. (2002). Prospective isolation of human clonogenic common myeloid progenitors. Proc. Natl. Acad. Sci. U S A *99*, 11872–11877.

Marr, C., Strasser, M., Schwarzfischer, M., Schroeder, T., and Theis, F.J. (2012). Multi-scale modeling of GMP differentiation based on single-cell genealogies. FEBS J. *279*, 3488–3500.

Matis, J.H., and Wehrly, T.E. (1990). Generalized stochastic compartmental models with Erlang transit times. J. Pharmacokinet. Biopharm. *18*, 589–607.

Newton, M.A., Guttorp, P., Catlin, S., Assun c c ão, R., and Abkowitz, J.L. (1995). Stochastic modeling of early hematopoiesis. J. Am. Stat. Assoc. *90*, 1146–1155.

Notta, F., Zandi, S., Takayama, N., Dobson, S., Gan, O.I., Wilson, G., Kaufmann, K.B., McLeod, J., Laurenti, E., Dunant, C.F., et al. (2016). Distinct routes of lineage development reshape the human blood hierarchy across ontogeny. Science *351*, aab2116.

Østby, I., Rusten, L.S., Kvalheim, G., and Grøttum, P. (2003). A mathematical model for reconstitution of granulopoiesis after high dose chemotherapy with autologous stem cell transplantation. J. Math. Biol. *47*, 101–136.

Pronk, C.J.H., Rossi, D.J., Månsson, R., Attema, J.L., Norddahl, G.L., Chan, C.K.F., Sigvardsson, M., Weissman, I.L., and Bryder, D. (2007). Elucidation of the phenotypic, functional, and molecular topography of a myeloerythroid progenitor cell hierarchy. Cell Stem Cell *1*, 428–442.

Reynaud, D., Lefort, N., Manie, E., Coulombel, L., and Levy, Y. (2003). In vitro identification of human pro-B cells that give rise to macrophages, natural killer cells, and T cells. Blood *101*, 4313–4321.

Roeder, I., Herberg, M., and Horn, M. (2009). An "age"-structured model of hematopoietic stem cell organization with application to chronic myeloid leukemia. Bull. Math. Biol. *71*, 602–626.

Sanjuan-Pla, A., Macaulay, I.C., Jensen, C.T., Woll, P.S., Luis, T.C., Mead, A., Moore, S., Carella, C., Matsuoka, S., Bouriez Jones, T., et al. (2013). Platelet-biased stem cells reside at the apex of the haematopoietic stem-cell hierarchy. Nature *502*, 232–236.

Schwartz, L. (1965). On Bayes Procedures (Zeitschrift für Wahrscheinlichkeitstheorie und Verwandte Gebiete). https://doi.org/10.1007/bf00535479.

Stapor, P., Weindl, D., Ballnus, B., Hug, S., Loos, C., Fiedler, A., Krause, S., Hroß, S., Fröhlich, F., Hasenauer, J., and Wren, J. (2018). PESTO: parameter EStimation TOolbox. Bioinformatics *34*, 705–707.

Strasser, M.K., Hoppe, P.S., Loeffler, D., Kokkaliaris, K.D., Schroeder, T., Theis, F.J., and Marr, C. (2018). Lineage marker synchrony in hematopoietic genealogies refutes the PU.1/GATA1 toggle switch paradigm. Nat. Commun. *9*, 2697.

Takano, H., Ema, H., Sudo, K., and Nakauchi, H. (2004). Asymmetric division and lineage commitment at the level of hematopoietic stem cells: inference from differentiation in daughter cell and granddaughter cell pairs. J. Exp. Med. *199*, 295–302.

Velten, L., Haas, S.F., Raffel, S., Blaszkiewicz, S., Islam, S., Hennig, B.P., Hirche, C., Lutz, C., Buss, E.C., Nowak, D., et al. (2017). Human haematopoietic stem cell lineage commitment is a continuous process. Nat. Cell Biol. *19*, 271–281.

Villaverde, A.F., and Banga, J.R. (2017). Dynamical compensation and structural identifiability of biological models: analysis, implications, and reconciliation. PLoS Comput. Biol. *13*, e1005878.

Villaverde, A.F., Evans, N.D., Chappell, M.J., and Banga, J.R. (2019). Input-Dependent structural identifiability of nonlinear systems. IEEE Control Syst. Lett. *3*, 272–277.

Watcham, S., Kucinski, I., and Gottgens, B. (2019). New insights into hematopoietic differentiation landscapes from single-cell RNA sequencing. Blood *133*, 1415–1426.

Weinreb, C., Wolock, S., Tusi, B.K., Socolovsky, M., and Klein, A.M. (2018). Fundamental limits on dynamic inference from single-cell snapshots. Proc. Natl. Acad. Sci. U S A *115*, E2467–E2476.

Xu, J., Wang, Y., Guttorp, P., and Abkowitz, J.L. (2018). Visualizing hematopoiesis as a stochastic process. Blood Adv. *2*, 2637–2645.

iScience, Volume *24*

Supplemental Information

Computational modeling of stem and progenitor cell kinetics identifies plausible hematopoietic lineage hierarchies

Lisa Bast, Michèle C. Buck, Judith S. Hecker, Robert A.J. Oostendorp, Katharina S. Götze, and Carsten Marr

Supplemental Information

Supplemental Data Items

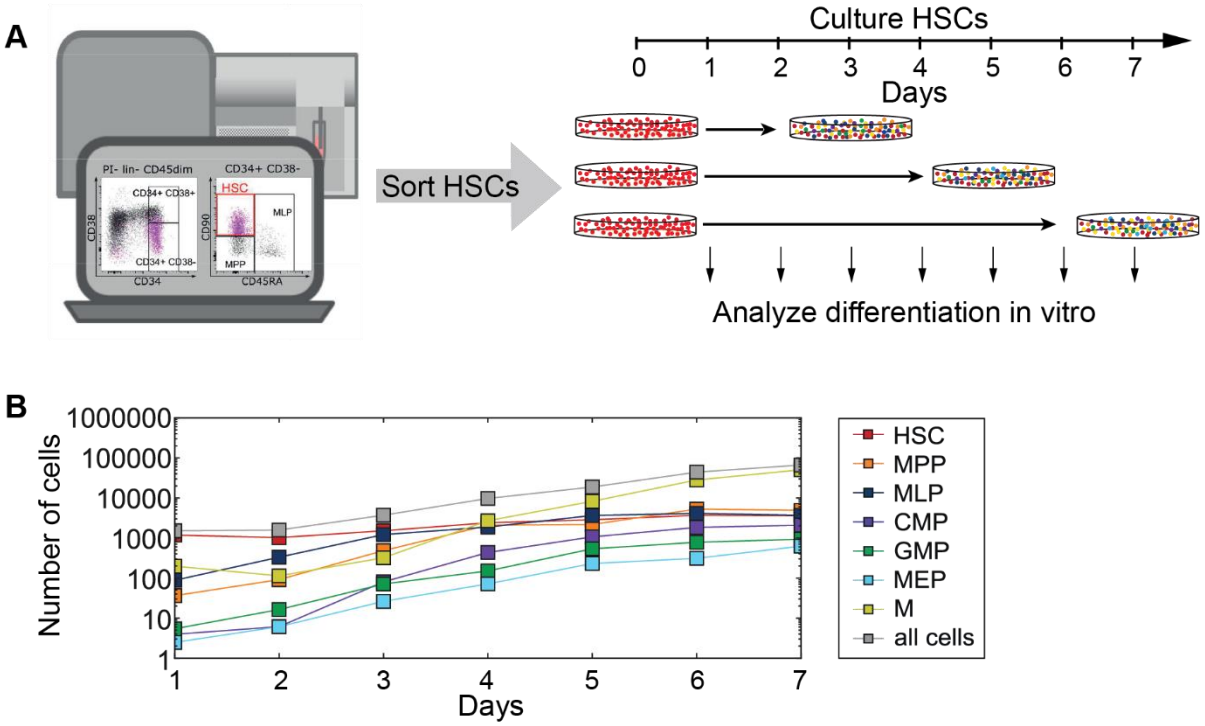

Figure S1. Measuring number of cells over time, Related to Figure 1 and Figure 3.
(A) Bone marrow cells from 10 donors were isolated. Each sample was purified by multiparameter immunophenotyping (FACS) for a HSC starting population which was then divided and cultured in several wells in parallel. Cell cultures were measured with FACS to observe cell abundances and division distribution of cultured bulk cells at subsequent measurement timepoints.
(B) Measured cell abundances for all seven cell type compartments (HSC, MPP, MLP, CMP, GMP, MEP, M) over time (connected dots) for one exemplary sample (ID 7).

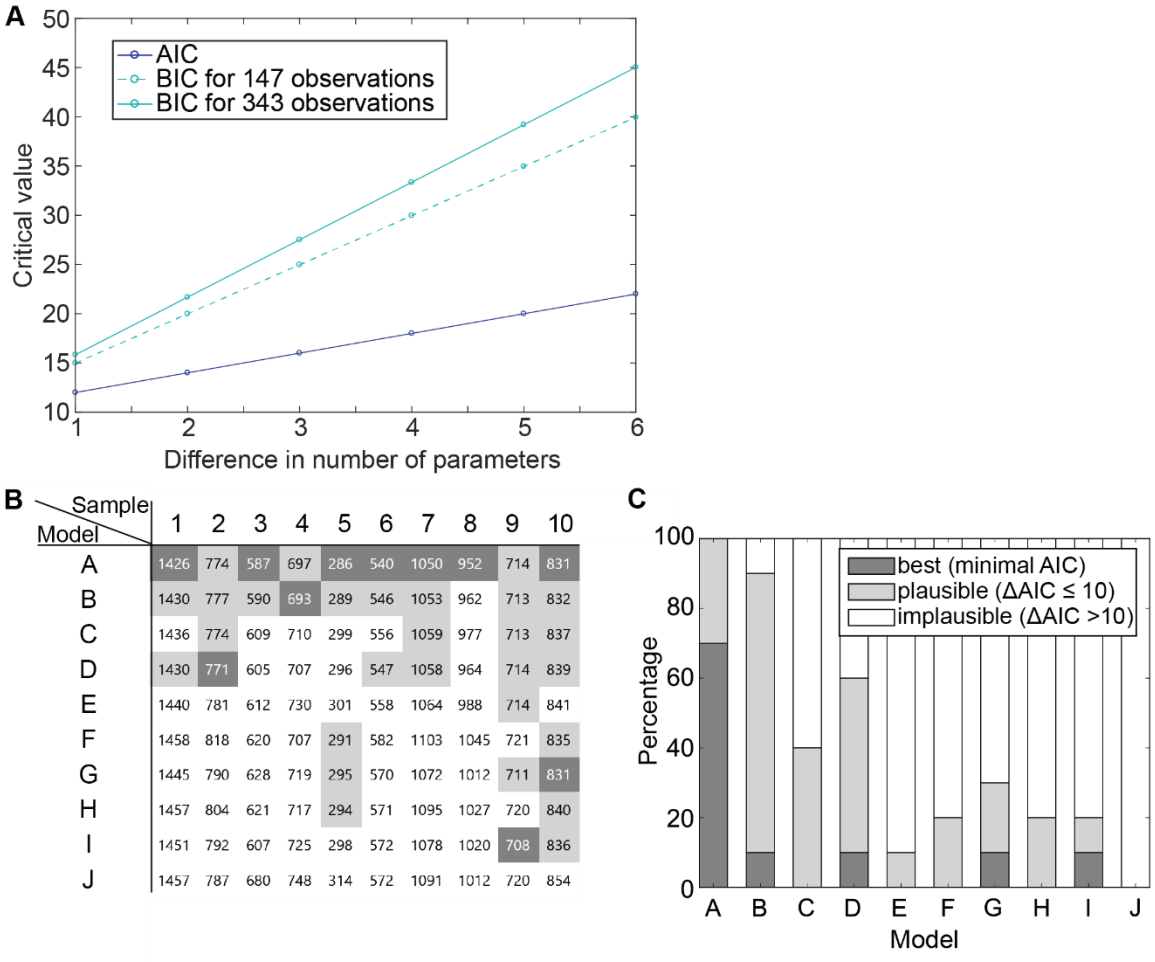

Figure S2. AIC identifies similar plausible models as BIC, Related to Figure 3.

(A) Critical values for BIC and AIC for rejecting a model over another less complex model for a difference in number of parameters of 1 to 6 are shown for the upper and lower boundary of observations. BIC shows larger critical values and is thus always a more conservative criterion compared to AIC.

(B) AIC values per model A-J (rows) for every individual sample (columns). Models were categorized into best (for the lowest AIC score), plausible (a difference to the lowest score ≤ 10) and implausible (a difference to the lowest score ≥ 10) for each sample.

(C) Relative frequency of a model to belong to one of the three categories (best, plausible, implausible) according to the AIC obtained from the 10 samples.

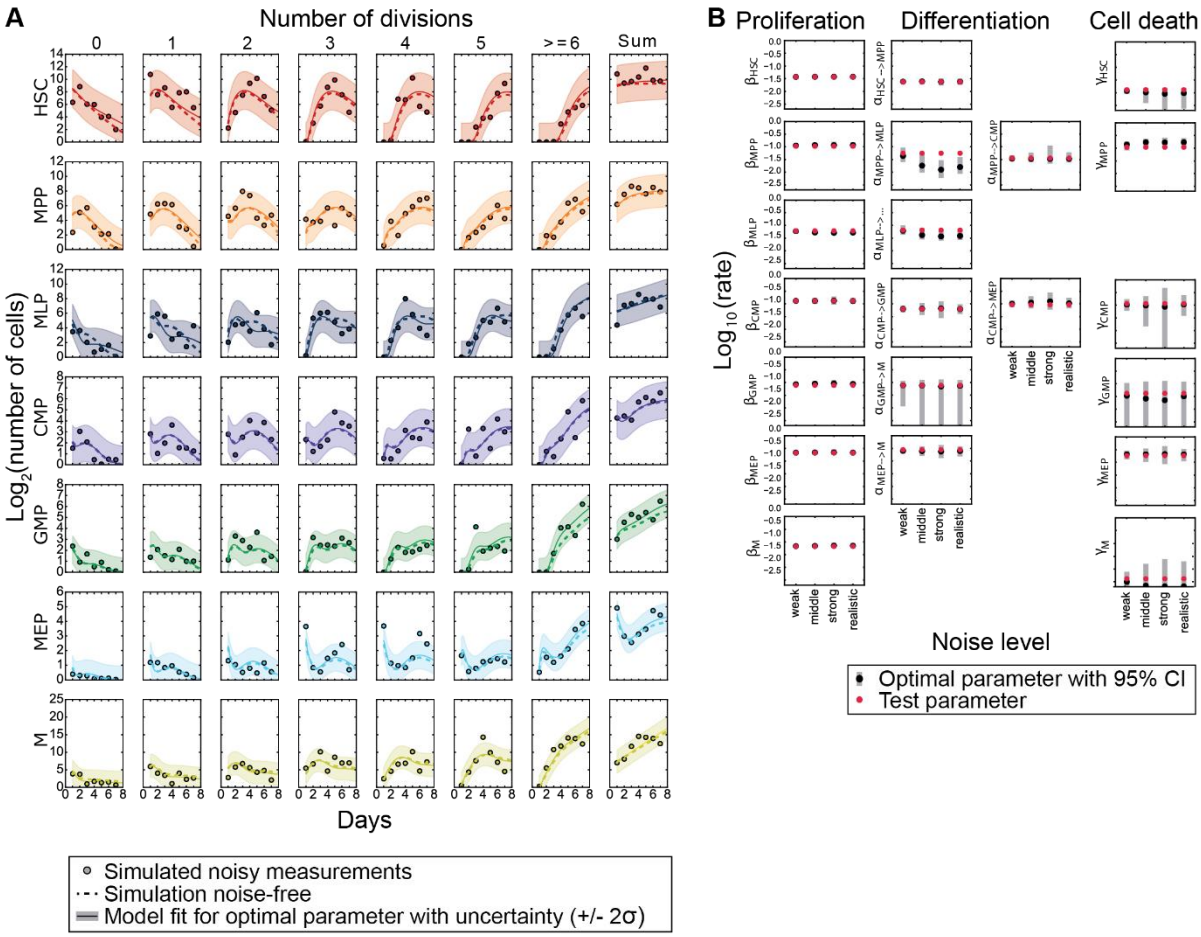

Figure S3. Exemplary model simulation and fitting, Related to Figure 4.

(A) Cell abundances of 49 compartments (first 7 columns) and sum over all divisions (last column) for each cell type. Model A was used to generate in silico data for a realistic test parameter (dots) and perturbed by cell compartment specific log-normal noise (shown for realistic noise level, $\sigma \in [0.6,1.1]$). Underlying (noise free) model observables (dashed line) and the model observables for the optimal parameter (solid line) deviate only slightly for the assumed noise level ($\pm 2\sigma$ error band).

(B) True parameter values (red dots) for which perturbed samples were simulated by using model A are for most rates contained in 95% confidence interval (grey boxes) of inferred parameter values (black dots) and deviate only slightly from the true value even for higher noise levels. The noise level for perturbation of simulated values was varied and set to σ= 0.4 for weak, σ= 0.8 for middle, σ=1.2 for strong, and $\sigma \in [0.6,1.1]$ for realistic noise.

Cell type(s)	Marker	Published in
HSC *	Lin$^-$ CD34$^+$ CD38$^-$ CD90$^+$ CD45RA$^-$	(Doulatov et al., 2010; Majeti et al., 2007)
HSC	Lin$^-$ CD34$^+$ CD38$^-$ CD45RA$^-$ CD90$^+$; CD49f$^+$	(Notta et al., 2011)
HSCs/ MPPs	CD133$^+$ CD34$^+$ CD45RA$^-$	(Görgens et al., 2013)
MPP *	Lin$^-$ CD34$^+$ CD38$^-$ CD90$^-$ CD45RA$^-$	(Doulatov et al., 2010; Majeti et al., 2007)
MPP	CD34$^+$ CD10$^-$ CD38$^-$ CD90$^-$ CD45RA$^-$	(Ostendorf et al., 2018)
CMP *	Lin$^-$ CD34$^+$ CD38$^+$ CD45RA$^-$ CD123$^+$	(Manz et al., 2002)
CMP	Lin$^-$ CD34$^+$ CD38$^+$ CD45RA$^-$ Flt3$^+$ CD7$^-$ CD10$^-$	(Doulatov et al., 2010)
GMP *	Lin$^-$ CD34$^+$ CD38$^+$ CD45RA$^+$ CD123$^+$	(Manz et al., 2002)
GMP	Lin$^-$ CD34$^+$ CD38$^+$ CD45RA$^+$ Flt3$^+$ CD7$^-$ CD10$^-$	(Doulatov et al., 2010)
MEP *	Lin$^-$ CD34$^+$ CD38$^+$ CD45RA$^-$ CD123$^-$	(Manz et al., 2002)
MEP	Lin$^-$ CD34$^+$ CD38$^+$ CD45RA$^-$ Flt3$^-$ CD7$^-$ CD10$^-$	(Doulatov et al., 2010)
Lymphoid/DC-restricted progenitors	CD34$^+$ Lin$^-$ CD10$^+$	(Galy et al., 1995)
MLP *	Lin$^-$ CD34$^+$ CD38$^-$ CD90$^{neg–lo}$ CD45RA$^+$	(Doulatov et al., 2010)
CLP	Lin$^-$, CD34$^+$, CD127$^+$	(Pang et al., 2011)
lympho-myeloid	CD133$^+$ CD34$^+$ CD45RA$^+$	(Görgens et al., 2013)
erythro-myeloid	CD133^{low} CD34$^+$ CD45RA$^-$	(Görgens et al., 2013)

Table S1: Commonly used gating strategies for identifying human hematopoietic stem and progenitor cells, Related to Figure 1. Strategies marked with * served as the basis for this study**.**

Parameter	Boundaries
$\beta_{S_j}, \gamma_{S_j}, \alpha_{S_{j1}\to S_{j2}}$, where $S_j, S_{j1}, S_{j2} \in \mathscr{S}$	$\left[\frac{1}{500}, 1\right] h^{-1}$
x_0	$\left[\min_r \left\{y^{\mathscr{D}}_{1,0}(t_1)\right\}, N_{input}\right]$, if $j = 1$ (for HSCs)
x_0	$\left[0, \max_r \left\{y^{\mathscr{D}}_{j,0}(t_1)\right\} + 0.1 * \max_r \left\{y^{\mathscr{D}}_{j,0}(t_1)\right\}\right]$, if $j > 1$ (other cell type compartments)

Table S2: Parameter boundaries used for fitting models A-J to experimental data, Related to Figure 2.

Parameter	**Individual ID (age, sex)**									
	1 (63, m)	**2 (57,m)**	**3 (70,m)**	**4 (63, m)**	**5 (51, m)**	**6 (26, m)**	**7 (29, m)**	**8 (44, m)**	**9 (24, m)**	**10 (76, w)**
$\alpha_{HSC \to MPP}$	-1.90 [-1.97, -1.83]	-1.72 [-1.79, -1.66]	-2.7 [-2.7, -2.52]	-1.47 [-1.57, -1.37]	-1.73 [-1.89, -1.57]	-1.61 [-1.74, -1.51]	-1.42 [-1.52, -1.32]	-1.47 [-1.54, -1.41]	-1.83 [-1.92, -1.73]	-1.62 [-1.74, -1.5]
β_{HSC}	-1.71 [-1.73, -1.68]	-1.64 [-1.67, -1.61]	-1.49 [-1.53, -1.46]	-1.45 [-1.5, -1.41]	-1.55 [-1.6, -1.49]	-1.32 [-1.38, -1.24]	-1.28 [-1.33, -1.22]	-1.35 [-1.38, -1.32]	-1.57 [-1.6, -1.54]	-1.52 [-1.55, -1.49]
γ_{HSC}	-2.48 [-2.70, -2.12]	-2.08 [-2.49, -1.67]	-1.43 [-1.5, -1.35]	-1.83 [-1.99, -1.72]	-1.51 [-1.72, -1.33]	-1.96 [-2.7, -1.7]	-2.7 [-2.7, -1.92]	-2.7 [-2.7, -2.28]	-2.07 [-2.57, -1.86]	-2.07 [-2.43, -1.72]
$\alpha_{MPP \to MLP}$	-1.33 [-1.50, -1.15]	-1.43 [-1.58, -1.27]	-2.7 [-2.7, -2.29]	-1.2 [-1.34, -1.04]	-2.7 [-2.7, -2.3]	-1.38 [-1.55, -1.24]	-0.97 [-1.21, -0.73]	-0.99 [-1.19, -0.79]	-1.34 [-1.57, -1.11]	-1.27 [-1.54, -1]
$\alpha_{MPP \to CMP}$	-1.14 [-1.32, -0.96]	-1.42 [-1.55, -1.28]	-2.7 [-2.7, -2.2]	-2.7 [-2.7, -2.53]	-2.7 [-2.7, -2.16]	-1.37 [-1.53, -1.12]	-1.32 [-1.49, -1.15]	-1.37 [-1.52, -1.23]	-1.49 [-1.72, -1.2]	-1.93 [-2.06, -1.8]
β_{MPP}	-1.26 [-1.31, -1.19]	-1.26 [-1.31, -1.2]	-1.28 [-1.32, -1.23]	-1.07 [-1.15, -0.98]	-0.85 [-1.05, -0.57]	-0.95 [-1.04, -0.85]	-1.21 [-1.44, -0.99]	-0.95 [-1.04, -0.86]	-1.22 [-1.3, -1.15]	-1.1 [-1.22, -0.98]
γ_{MPP}	-2.70 [-2.70, -2.29]	-2.7 [-2.7, -1.2]	-2.7 [-2.7, -2.11]	-1.32 [-1.67, -1]	-0.77 [-1.02, -0.49]	-2.7 [-2.7, -2.15]	-1.42 [-1.89, -0.96]	-1.3 [-1.95, -0.65]	-2.7 [-2.7, -1.37]	-1.03 [-1.42, -0.64]
α_{MLP}	-1.04 [-1.36, -0.77]	-1.06 [-1.3, -0.82]	-2.7 [-2.7, -1.91]	-0.79 [-0.99, -0.61]	-2.7 [-2.7, -1.91]	-2.7 [-2.7, -2.36]	-1.3 [-1.49, -1.11]	-1.36 [-1.53, -1.2]	-0.98 [-1.41, -0.67]	-1.19 [-1.46, -0.92]
β_{MLP}	-1.32 [-1.42, -1.21]	-1.39 [-1.59, -1.2]	-1.41 [-1.44, -1.36]	-1.08 [-1.23, -0.95]	-1.5 [-1.56, -1.44]	-1.13 [-1.2, -1.03]	-1.28 [-1.38, -1.19]	-1.15 [-1.24, -1.07]	-1.23 [-1.41, -1.05]	-1.27 [-1.41, -1.14]
$\alpha_{CMP \to GMP}$	-1.88 [-1.97, -1.78]	-1.48 [-1.76, -1.21]	-2.7 [-2.7, -2.27]	-1.71 [-1.86, -1.58]	-1.63 [-2.04, -1.43]	-1.51 [-1.68, -1.32]	-1.09 [-1.32, -0.85]	-1.19 [-1.4, -0.98]	-0.43 [-0.68, -0.17]	-2.7 [-2.7, 0]
$\alpha_{CMP \to MEP}$	-1.14 [-1.39, -0.42]	-0.63 [-0.88, -0.37]	-2.7 [-2.7, -1.93]	-1.77 [-1.87, -1.65]	-1.54 [-2.7, -1.29]	-0.84 [-1.24, -0.39]	-1.27 [-1.49, -1.05]	-1.02 [-1.21, -0.84]	-1.44 [-1.78, -0.79]	-2.7 [-2.7, 0]
β_{CMP}	-1.15 [-1.51, -0.88]	-0.99 [-1.18, -0.8]	-1.34 [-1.37, -1.31]	-1.19 [-1.25, -1.13]	-1.43 [-1.58, -1.3]	-0.41 [-0.7, -0.11]	-1.03 [-1.16, -0.9]	-0.85 [-0.99, -0.72]	-0.83 [-1.73, -0.45]	-1.13 [-1.28, -0.98]
γ_{CMP}	-0.36 [-1.62, -0.12]	-2.7 [-2.7, 0]	-2.7 [-2.7, -2.05]	-2.7 [-2.7, -2.17]	-2.7 [-2.7, -1.38]	-0.28 [-0.71, 0]	-2.7 [-2.7, -1.59]	-2.7 [-2.7, -1.25]	-0.5 [-2.7, 0]	-2.7 [-2.7, 0]
$\alpha_{GMP \to M}$	-2.70 [-2.70,	-2.7 [-2.7,	-2.7 [-2.7,	-1.26 [-1.52,	-2.7 [-2.7,	-2.7 [-2.7,	-2.7 [-2.7,	-2.7 [-2.7,	-0.5 [-0.76,	-2.7 [-2.7,

	-1.94]	0]	-1.63]	-1.08]	-0.44]	-1.18]	-1.28]	-0.43]	-0.1]	0]
β_{GMP}	-1.37 [-1.44, -1.22]	-1.2 [-1.5, -0.89]	-1.37 [-1.45, -1.31]	-1.02 [-1.13, -0.92]	-1.26 [-2.7, -0.4]	-1.05 [-1.16, -0.91]	-1.1 [-1.34, -0.85]	-0.99 [-1.24, -0.75]	-1.11 [-1.72, -0.57]	-1.44 [-1.5, -1.38]
γ_{GMP}	-2.70 [-2.70, -1.93]	-1.02 [-1.58, -0.46]	-1.81 [-2.7, -1.53]	-2.7 [-2.7, -1.21]	-0.82 [-1.18, -0.11]	-2.7 [-2.7, -1.11]	-0.88 [-1.16, -0.6]	-0.96 [-1.26, -0.67]	-2.7 [-2.7, 0]	-2.7 [-2.7, 0]
$\alpha_{MEP\rightarrow M}$	-0.68 [-1.28, -0.36]	0 [-0.25, 0]	-2.7 [-2.7, -2.19]	-2.7 [-2.7, -2.15]	-2.7 [-2.7, -0.64]	-0.8 [-1.36, -0.41]	-2.7 [-2.7, -1.07]	-0.6 [-0.87, -0.34]	-2.7 [-2.7, -0.02]	-1.58 [-2.4, -0.75]
β_{MEP}	-1.11 [-1.59, -0.77]	-0.41 [-0.86, 0]	-1.4 [-1.44, -1.35]	-1.24 [-1.32, -1.17]	-1.22 [-1.65, -0.54]	-0.98 [-1.49, -0.67]	-1.04 [-1.23, -0.84]	-0.74 [-0.92, -0.55]	-2.13 [-2.7, -1.31]	-1.27 [-1.41, -1.14]
γ_{MEP}	-1.11 [-2.70, 0]	-0.08 [-0.65, 0]	-2.7 [-2.7, -2.14]	-2.7 [-2.7, -2.05]	-0.95 [-1.29, -0.35]	-1.3 [-2.7, -0.44]	-0.85 [-1.12, -0.58]	-1.34 [-2.27, -0.41]	-2.7 [-2.7, -0.49]	-2.17 [-2.7, 0]
β_{M}	-1.48 [-1.52, -1.44]	-1.1 [-1.23, -0.98]	-1.19 [-1.23, -1.15]	-1.22 [-1.26, -1.16]	-1.2 [-1.25, -1.13]	-1.16 [-1.23, -1.09]	-1.32 [-1.36, -1.28]	-1.2 [-1.26, -1.13]	-1.04 [-1.13, -0.96]	-1.34 [-1.39, -1.29]
γ_{M}	-2.70 [-2.70, -2.31]	-2.7 [-2.7, 0]	-2.7 [-2.7, -2.18]	-2.7 [-2.7, -2.49]	-2.58 [-2.7, -1.72]	-2.7 [-2.7, -2.16]	-2.7 [-2.7, -2.17]	-2.7 [-2.7, -1.67]	-2.7 [-2.7, -1.79]	-2.7 [-2.7, -0.91]

Table S3: Log_{10} transformed parameter values with their 95% profile likelihood-based confidence intervals in [cells/h] resulting from fitting model A to each of the 10 individuals, Related to Figure 3.

Transparent Methods

Derivation of the set of lineage hierarchy models tested

Based on the classical model of hematopoiesis (model A, Figure 1A) and recently reported experimental evidence, we derived nine alternative models, likewise containing compartments HSC, MPP, CMPs, MLP, MEP, GMP, and M, but with different direct differentiation transitions between them (Figure 1B-J). The restriction on 7 cell types is determined by the number of discernable populations in flow cytometry. Furthermore, our setup does not allow to depict myeloid and lymphoid differentiation past the HSPC compartment: Whereas conditions allowing in vitro differentiation of HSCs into mature myeloid cells are well established, it is much more difficult to culture mature lymphoid cells past the committed progenitor stage which requires a specific culture medium using a cloned stromal feeder layer (i.e. Whitlock-Witte culture).

Several studies in humans (Doulatov et al., 2010; Doulatov et al., 2012; Giebel et al., 2006; Reynaud et al., 2003; Goardon et al., 2011; Rossi et al., 2008; Hao et al., 2001) show that progenitor cells in the CD34+CD38− compartment, which are CD90+ (Thy1) and CD45RA+, correspond to multipotent lymphoid progenitor cells (MLP), and have lymphoid, macrophage, and dendritic potential. As these results suggest that MLPs can also differentiate to GMPs, we have incorporated this transition in models B, C, E and I (Figure 1B,C,E,I).

In a study investigating adult blood lineage commitment in mice (Adolfsson et al., 2005), the authors proposed a revised model of hematopoiesis. They identified a new cell type, the lymphoid-primed

multipotent progenitors (LMPPs), which are FLT3+ Lin^- $Sca\text{-}1^+$ $c\text{-}Kit^+$ cells (LSK Flt3+ cells), that possess B-cell, T-cell and granulocyte-monocyte (GM) potential but lack megakaryocyte-erythrocyte (MegE) potential. Mouse LSK cells include long-term HSCs, short-term HSCs, and MPPs. The existence of a distinct LSK subtype that does not have MegE potential may indicate that MEPs can directly arise from HSCs. Furthermore, loss of MegE potential in the newly defined LMPP compartment indicates a direct LMPP to GMP transition, without differentiation into CMPs first. In this model, HSCs can generate LMPPs with lymphocyte and GM potential, and CMPs with MegE and GM potential. These findings led on the one hand to the possible direct transition from the HSC to CMP compartment and from MPPs to GMPs in models F and H (Figure 1F,H), and on the other hand to a transition between the HSC and MEP compartment in models E, G and I (Figure 1E,G,I). The direct differentiation path from HSCs to MEPs (Figure 1E,G,I) was also supported by in vitro studies of Takano et al. (2004), who investigated colony forming units of LSK daughter and granddaughter cells. However, a separate study from (Forsberg et al., 2006) also investigated the lineage potential of FLT3+ LMPPs but found conflicting results, which instead support the classical model of hematopoiesis (model A, Figure 1A).
In another mouse study, a fraction of phenotypically defined HSCs was shown to express von Willebrand factor (vWF), a protein mainly expressed by platelets and endothelium (Månsson et al., 2007). The existence of a megakaryocyte-primed HSC subset was also experimentally investigated by Sanjuan-Pla et al. (2013) generating vWF-eGFP transgenic mice, isolating LSK $CD150^+$ $CD48^-$ $CD34^-$ HSCs with a high eGFP expression and transplanting them into irradiated mice. They found that vWF-eGFP+ HSCs were platelet biased, additionally contributing to other myeloid lineages whereas their lymphoid contribution was very marginal.
Models E and H furthermore include the direct differentiation path from MPPs to MEPs, which was suggested by Pronk et al. (2007) (Figure 1E,H). By studying the phenotypic, functional and molecular characteristics of myeloerythroid precursors, they identified MPPs which give rise to erythroid and megakaryocytic progeny through various intermediate stages.This finding is supported by human studies, in which BAH1 and CD71 were identified as erythroid and megakaryocytic differentiation markers within the CD34+ CD38- MPP compartment (Notta et al., 2016).

Sample collection and storage

Healthy BM samples were obtained from allogeneic donor BM filters or from femoral heads of patients undergoing hip replacement surgery. Written informed consent in accordance with the Declaration of Helsinki was obtained from all patients according to protocols approved by the ethics committee of the Technische Universität München (approval number 538/16).
Mononuclear cells were isolated by ficoll gradient density centrifugation. Cells were frozen in 10 % DMSO (Serva, Cat: 20385) and 90 % heat inactivated FCS (Merck, Cat: S0115), $5x10^7$ cells/ml) at -80°C using a freezing chamber maintaining a controlled freezing rate of approximately 1°C per minute. Samples were stored in a N2 biobank until further use.

Antibody staining and FACS-sorting

For the sorting procedure of HSCs, MNC cells were thawed and immediately placed into IMDM (1x) + GlutaMAX (Gibco, Cat: 31980-022). Dead cells were removed by density gradient centrifugation. MNC were washed with 2 ml PBS and centrifuged. For the ability to track cell divisions in later FACS analysis, pellets were mixed with 2 ml of 1 µM CellTrace™ Violet stain (ThermoFisher Scientific, Cat: C34557) in PBS (37°C) and incubated for 20 min at 37°C. The reaction was stopped by adding 10 ml ice-cold HF2 medium containing 1xHBSS (Gibco, Cat:14185-045), 2 % heat-inactivated FCS (Biochrom, Cat:S0115), 0.01 M HEPES (Gibco, Cat: 15630-056), and 100 U/ml Pen/Strep (Gibco, Cat: 15140-122). After incubating 5 min on ice, cells were centrifuged and antibody staining was performed. Cells were first incubated with biotin-coupled antibodies, including 1 µl of each anti-CD4 (BioLegend, Clone: RPA-T4, Cat: 300504), anti-CD8a (BioLegend, Clone: RPA-T8, Cat: 301004), anti-CD15 (BioLegend, Clone: H198, Cat: 323016), anti-CD19 (BioLegend, Clone: H1BT9, Cat: 302204), and anti-CD235a (eBioscience, Clone: HIR2, Cat: 13-9987-82). for 20 min, on ice in the dark and then centrifuged (1500 rpm, 5 min). Pellets were resuspended with 100 µl of fluorescence-coupled antibody mix, including 5 µl anti-CD34-FITC (BD, Clone: 581, Cat: 555821), 5µl anti-CD90-PE (eBioscience, Clone: 5E10, Cat: 12-0909-42), 5 µl anti-CD123-BV510 (BioLegend, Clone: 6H6, Cat: 306021), 2.5 µl anti-CD38-APC (BD, Clone: HB7, Cat: 345807), 2.5 µl anti-CD45RA-PE-Cy7 (BD, Clone: HI100, Cat: 560675), 1 µl CD45-PeCy5.5 (BioLegend, Clone: HI30, Cat: 304028), and 1 µl APC/Cy7-Streptavidin (BioLegend, Cat: 405208) and incubated for 40 min on ice and in the dark. Pellets were resuspended in 500 µl HF2 with 0.2 µg propidium iodide and filtered using a 40 µm cell strainer. The sorting procedure was performed on a BD FACSAria™ III equipped with 4 lasers (488 nm, 405 nm, 561 nm, 635 nm).

Analysis of cell compartments on days 1 to 7, cultured cells were harvested, centrifuged and antibody staining was performed as described for the sorting procedure. Additionally, 50 µl of Flow-Count Fluorospheres (Beckman Coulter, Cat: 7547053) were added. FACS analysis was performed on a BeckmanCoulter CyAn, equipped with 405nm, 488nm, and 633 nm lasers. Compensation and gating was performed using the FlowJo V10 software (FlowJo LLC, Ashland, OR). Cell divisions were estimated by the decreasing intensity of the CellTrace™ Violet fluorophore.

Cell culture

Sorted HSCs (Lin-CD34+CD38-CD90+CD45RA-) were cultured at a concentration of $2.5x10^3$ cells/ml in serum-free medium (80% IMDM(1x)+GlutaMAX (Gibco, Cat: 31980-022) and 20 % BIT9500 (StemCell Technologies, Cat: 09500)) freshly supplemented with 10µM 2-Mercaptoethanol (Gibco, Cat: 31350-010), 8 µg/ml Ciprofloxacin (CiproHEXAL 200mg/100ml), 4 µg/ml LDL (StemCell Technologies, Cat: 02698), 100 ng/ml SCF (R&D Systems, Cat: 255-SC), 100ng/ml FLT3-Ligand (R&D Systems, Cat 308-FK), 25 ng/ml TPO (R&D Systems, Cat: 288-TP), 10 ng/ml IL3 (R&D Systems, Cat: 203-IL), 10ng/ml IL6 (R&D Systems, Cat: 206-IL) , 50 ng/ml GM-CSF (R&D Systems, Cat: 215-GM), 50 ng/ml G-CSF (Filgrastim, Hexal), and 2U/ml erythropoietin (Janssen, PZN: 00878122). Cells were cultured at 37°C with 5 % CO_2.

Computational approach

To assess the plausibility of a set of previously suggested lineage hierarchies for healthy human hematopoiesis, we derived a computational modeling approach. Based on a selection of previously suggested lineage hierarchies, we mechanistically modeled the cell differentiation dynamics. In the following, we consider the cell types hematopoietic stem cells (HSCs), multipotent progenitor cells (MPPs), common myeloid progenitors (CMPs), multipotent lymphocyte progenitors (MLPs), megakaryocyte erythrocyte progenitors (MEPs), granulocyte monocyte progenitors (GMPs) and mature and late progenitors (M) as species $\mathcal{S} = \{HSC, MPP, MLP, CMP, GMP, MEP, M\}$, for which division distributions and counts were experimentally observed at time points $\underline{t_0, ..., t_{n_t}}$ (Figure S1B-C). We consider a set of 10 biologically motivated lineage hierarchies (Figure 1A-J) and derive a mathematical model for each of them (Figure 2A). The 10 models are then used to analyse which lineage hierarchies are plausible and which ones can be rejected based on our experimental data.

Mechanistic models of cell differentiation dynamics

To mechanistically model human blood cell production, we compiled lineage hierarchies suggested in the literature. Each hierarchy is a biochemical reaction network in which the species $\underline{\mathcal{S}}$ are given by the cell types observed in the experiment. Cell differentiation, proliferation, and death are defined as cell type specific reactions. For MLPs the outflux reaction is defined as net differentiation and describes differentiation combined with cell death to ensure structural parameter identifiability. Note that each model considers the same proliferation and cell death reactions but a different set of differentiation reactions (Table 2). These can be derived from the respective model scheme of the set of plausible lineage hierarchies (Figure 1A-J) and are given by the cell types observed in the experiment. Cell differentiation, proliferation, and death are defined as cell type specific reactions (Table 1), where reactions $R_1 - R_7$ and $R_{22} - R_{27}$ which describe proliferation and cell death are present in all models. The model complexity, which corresponds to the number of reaction rates varies between models A-J (Table 2). The respective ODE systems derived from the reactions above describe the evolution of the cell concentrations over time for each compartment of a particular model. Differentiation and cell death reduces and proliferation increases the number of cells within the compartment proportionally to the cell concentration of this compartment at time t. The ODE system for model A without considering division compartments or intermediate states is given by

$$
\begin{aligned}
\dot{x}_1 &:= \frac{d[HSC]}{dt} = -(\alpha_{HSC\to MPP} - \beta_{HSC} + \gamma_{HSC})[HSC] \\
\dot{x}_2 &:= \frac{d[MPP]}{dt} = \alpha_{HSC\to MPP}[HSC] - (\alpha_{MPP\to CMP} + \alpha_{MPP\to MLP} - \beta_{MPP} + \gamma_{MPP})[MPP] \\
\dot{x}_3 &:= \frac{d[MLP]}{dt} = \alpha_{MPP\to MLP}[MPP] - (\alpha_{MLP\to\ldots} - \beta_{MLP})[MLP] \\
\dot{x}_4 &:= \frac{d[CMP]}{dt} = \alpha_{MPP\to CMP}[MPP] - (\alpha_{CMP\to GMP} + \alpha_{CMP\to MEP} - \beta_{CMP} - \gamma_{CMP})[CMP] \\
\dot{x}_5 &:= \frac{d[GMP]}{dt} = \alpha_{CMP\to GMP}[CMP] - (\alpha_{GMP\to M} - \beta_{GMP} + \gamma_{GMP})[GMP] \\
\dot{x}_6 &:= \frac{d[MEP]}{dt} = \alpha_{CMP\to MEP}[CMP] - (\alpha_{MEP\to M} - \beta_{MEP} + \gamma_{MEP})[MEP] \\
\dot{x}_7 &:= \frac{d[M]}{dt} = \alpha_{GMP\to M}[GMP] + \alpha_{MEP\to M}[MEP] - (\beta_M + \gamma_{MEP})[M]
\end{aligned} \tag{1}
$$

with initial condition $\mathbf{x}(0) = \mathbf{x}_0$.
In general, the ODE system is given by

$$
\dot{x}_j := \frac{dS_j}{dt} = \sum_{i\in I_j} \alpha_{i\to j} \cdot S_i(t) + \left(\beta_j - \gamma_j - \sum_{o\in O_j} \alpha_{j\to o}\right) \cdot S_j(t), \tag{2}
$$

$\forall j = 1, \ldots, |\mathcal{S}|$ where I_j is the set of influx compartments and O_j the set of outflux compartments of the respective species $S_j \in \mathcal{S}$ and the initial condition is given by $\mathbf{x}(0) = \mathbf{x}_0$.
Incorporating the information of the number of cell divisions N_{div}, the ODE system is expanded by introducing additional states which indicate not only the cell type but also the number of divisions occurring within the time interval of interest
$[t_0, t_i^{obs}]$ (Figure 2A). Hence, each ODE describes the evolution of cell abundances of species $S_j \in \mathcal{S}$ that divided $n_{div} \in \{0, \ldots, N_{div}\}$ times over time, which is denoted by $\frac{d[S_{j,n_{div}}]}{dt}$. This leads to an ODE system of $N_{div} \cdot n_c$ equations, where $n_c = 7$ is the number of cell type compartments. It is given by

$$
\begin{aligned}
\dot{x}_{(j-1)\cdot N_{div}+1} &:= \frac{dS_{j,0}(t)}{dt} = \sum_{i\in I_j} \alpha_{i\to j} \cdot S_{i,0}(t) + \left(\beta_j - \gamma_j - \sum_{o\in O_j} \alpha_{j\to o}\right) \cdot S_j(t) \\
\dot{x}_{(j-1)\cdot N_{div}+n_{div}+1} &:= \frac{dS_{j,n_{div}}(t)}{dt} = 2\beta_j \cdot S_{j,n_{div}-1}(t) + \sum_{i\in I_j} \alpha_{i\to j} \cdot S_{i,n_{div}}(t) - \left(\beta_j + \gamma_j + \sum_{o\in O_j} \alpha_{j\to o}\right) \cdot S_{j,n_{div}}(t) \\
\dot{x}_{j\cdot N_{div}} &:= \frac{dS_{j,N_{div}}(t)}{dt} = 2\beta_j \cdot S_{j,N_{div}-1}(t) + \sum_{i\in I_j} \alpha_{i\to j} \cdot S_{i,N_{div}}(t) + \left(\beta_j - \gamma_j - \sum_{o\in O_j} \alpha_{j\to o}\right) \cdot S_{j,N_{div}}(t)
\end{aligned} \tag{3}
$$

$\forall j = 1, \ldots, |\mathcal{S}|$ and $n_{div} = 0, 1, \ldots, N_{div}$. The waiting time for a differentiation, proliferation, or death event is anti-proportional to the corresponding reaction rate and follows an exponential distribution $T \sim \exp(r)$, where $r \in \{\alpha_{(.)}, \beta_{(.)}, \gamma_{(.)}\}$. This is in contrast with the observation that the considered processes (differentiation, proliferation, and cell death) require a minimum time to be completed. To more accurately describe transition times between cell states, we introduced intermediate states and further expanded the model (Figure 2A). By introducing intermediate states, the waiting time to stay in a particular state corresponds to the sum of exponentially distributed waiting times of its n_{IS} intermediate states and is thereby per definition Erlang(n_{IS},r) distributed (Matis and Wehrly, 1990).
The model allows to describe up to N_{div} division compartments per cell type compartment and if cells divide more often (more than N_{div} times), they accumulate in the N_{div}-compartment of the respective species S_j. In total it consists of

$$
N_{eq} = \begin{cases} N_{div} \cdot \left(\left(n_{IS} \cdot \sum_{j=1}^{|\mathcal{S}|} (n_j^{out} + 2)\right) + 1\right), & n_{IS} > 1 \\ N_{div} \cdot |\mathcal{S}|, & n_{IS} = 1 \end{cases} \tag{4}
$$

equations, where n_j^{out} is the number of outfluxes of compartment S_j and n_{IS} is the number of intermediate states within each compartment S_j.
Each ODE describes the time evolution of the number of cells of species $S_j \in \mathcal{S}$ that divided $n_{div} \in \{0, ..., N_{div}\}$ times and are in the k-th proliferation intermediate state, the l-th differentiation and the m-th cell death intermediate state, which is denoted by $\frac{d[S^{(k,l,m)}_{j,n_{div},i_o}(t)]}{dt}$ where $n_{div} = 0, ..., N_{div}, \quad i_o = 1, ..., n_j^{out}, \quad k, l, m = 1, ..., n_{IS}$ and $j = 1, ..., |\mathcal{S}|$.
The ODE system is given by

$$
\begin{aligned}
\frac{d[S^{(0,0,0)}_{j,n_{div},1}]}{dt} &:= \begin{cases}
n_{IS} \cdot \Big(\sum_{i \in I_j} \alpha_{i \to j} \cdot S^{(0,n_{IS},0)}_{i,n_{div},1}(t) \\
\quad -(\beta_j + \sum_{o \in O_j} \alpha_{j \to o} + \gamma_j) \cdot S^{(0,0,0)}_{j,n_{div},1}(t) \Big) & , \text{ if } n_{div} = 0 \\
n_{IS} \cdot \Big(\sum_{i \in I_j} \alpha_{i \to j} \cdot S^{(0,n_{IS},0)}_{i,n_{div},1}(t) \\
\quad -(\beta_j + \sum_{o \in O_j} \alpha_{j \to o} + \gamma_j) \cdot S^{(0,0,0)}_{j,n_{div},1}(t) \\
\quad +\beta_j \cdot S^{(n_{IS},0,0)}_{j,n_{div}-1,1}(t) \Big) & , \text{ if } n_{div} \in \{1, ..., N_{div}-1\} \\
n_{IS} \cdot \Big(\sum_{i \in I_j} \alpha_{i \to j} \cdot S^{(0,n_{IS},0)}_{i,n_{div},1}(t) \\
\quad -(\beta_j + \sum_{o \in O_j} \alpha_{j \to o} + \gamma_j) \cdot S^{(0,0,0)}_{j,n_{div},1}(t) \\
\quad +\beta_j \cdot S^{(n_{IS},0,0)}_{j,n_{div}-1,1}(t) + 2 \cdot \beta_j \cdot S^{(n_{IS},0,0)}_{j,n_{div},1}(t) \Big) & , \text{ if } n_{div} = N_{div}
\end{cases} \\
&= \dot{x}_{(j-1)\cdot(N_{div}\cdot(2\cdot n_{IS}+1)+\sum_{c=1}^{j-1} n_c^{out}\cdot n_{IS}\cdot N_{div}+(n_{div}+1)} \\
\frac{d[S^{(k,0,0)}_{j,n_{div},1}(t)]}{dt} &:= n_{IS} \cdot \beta_j \left(S^{(k-1,0,0)}_{j,n_{div},1}(t) - S^{(k,0,0)}_{j,n_{div},1}(t) \right) \\
&= \dot{x}_{(j-1)\cdot(N_{div}\cdot(2\cdot n_{IS}+1)+\sum_{c=1}^{j-1} n_c^{out}\cdot n_{IS}\cdot N_{div}+(n_{div}+k+1)} \\
\frac{d[S^{(0,0,m)}_{j,n_{div},1}]}{dt} &:= n_{IS} \cdot \gamma_j \left(S^{(0,0,m-1)}_{j,n_{div},1}(t) - S^{(0,0,m)}_{j,n_{div},1}(t) \right) \\
&= \dot{x}_{(j-1)\cdot(N_{div}\cdot(2\cdot n_{IS}+1)+\sum_{c=1}^{j-1} n_c^{out}\cdot n_{IS}\cdot N_{div}+(n_{div}+m+n_{IS}+1)} \\
\frac{d[S^{(0,l,0)}_{j,n_{div},i_o}]}{dt} &:= n_{IS} \cdot \alpha_{j \to i_o} \left(S^{(0,l-1,0)}_{j,n_{div},i_o}(t) - S^{(0,l,0)}_{j,n_{div},i_o}(t) \right) \\
&= \dot{x}_{(j-1)\cdot(N_{div}\cdot(2\cdot n_{IS}+1)+\sum_{c=1}^{j-1} n_c^{out}\cdot n_{IS}\cdot N_{div}+(n_{div}+l+i_o+2\cdot n_{IS}+1)}
\end{aligned} \tag{5}
$$

and initial condition $\mathbf{x}(0) = \mathbf{x}_0$.
Note that for both model extensions, the number of states increases, but the number of parameters stays constant.

Parameter inference

Our models contain between 29 and 35 unknown parameters $\boldsymbol{\theta} = (\theta_1, ..., \theta_{n_\theta})$, which are the reaction rates $\beta_{S_j}, \gamma_{S_j}, \alpha_{S_{j1} \to S_{j2}}$, where $S_j, S_{j1}, S_{j2} \in \mathcal{S}$ and the initial conditions are given by $\mathbf{x}(0) = \mathbf{x}_0(\theta)$, where

$$
\mathbf{x}_0(\theta) = S^{(k,l,m)}_{j,n_{div},i_o}(0) = \begin{cases} \theta_j, & \text{if } k = l = m = 0 \text{ and } n_{div} = i_o = 1 \\ 0, & \text{otherwise} \end{cases} \tag{6}
$$

for $j = 1, ..., |\mathcal{S}|$, and $i_{div} = 0, ..., 6$. These parameters are estimated by minimizing the weighted difference between observed and modeled cell counts by applying maximum likelihood estimation.
Let $\mathcal{M}(\theta)$ be a particular model consisting of dynamics $\dot{\mathbf{x}} = f(\mathbf{x}, \theta)$ and model observations $y^{\mathcal{M}} = h(x, \theta)$:

$$\mathscr{M}(\theta): \left\{ \begin{array}{l} \dot{\mathbf{x}} = f(\mathbf{x},\theta) = \left\{ \frac{d[S^{(k,l,m)}_{j,n_{div},i_o}](t)}{dt} \right\}, \ \mathbf{x}(0) = \mathbf{x}_0(\theta), \\ \mathbf{y}^{\mathscr{M}} = h(x,\theta) = \left\{ \sum_{k,l,m=0}^{n_{IS}} \sum_{i_o=1}^{n^{out}_j} [S^{(k,l,m)}_{j,n_{div},i_o}](t) \right\} \end{array} \right\}, \tag{7}$$

where $j = 1, ..., |\mathcal{S}|$, $k, l, m = 1, ..., n_{IS}$, $i_o = 1, ..., n^j_{out}$, $i_{div} = 1, ..., N_{div}$ and $w \in \{1, 2\}$ and let

$$\mathscr{D} = \left\{ t_s, y^{\mathscr{D}}_{j,n_{div}}(t_s) \right\}_{s=1,..,n_t,\ j=1,...,|\mathscr{S}|,\ n_{div}=1,...,N_{div}} \tag{8}$$

be the data (Figure S1B-C). Here $y^{\mathcal{D}}_{j,i_{div}}(t_s)$ denotes the vector of observed cell counts of species $j = 1, ..., |\mathcal{S}|$ that divided $i_{div} = 0, ..., N_{div}$ times at time t_s of a particular individual. For parameter estimation, we assumed the observations $y^{\mathcal{D}}_{j,i_{div}}(t_s)$ are subject to multiplicative log-normally distributed measurement noise

$$\begin{aligned} y^{\mathscr{D}}_{j,n_{div}}(t_s) &= y^{\mathscr{M}}_{j,n_{div}}(t_s) \cdot \nu, \text{ with } \nu \sim log\mathcal{N}(0, \sigma^2_{j,n_{div}}) \\ \log(y^{\mathscr{D}}_{j,n_{div}}(t_s)) &= \log(y^{\mathscr{M}}_{j,n_{div}}(t_s)) + \varepsilon, \text{ with } \varepsilon \sim \mathcal{N}(0, \sigma^2_{j,n_{div}}) \end{aligned} \tag{9}$$

due to counting errors (i.e. technical error of the FACS machine, see Methods) or false cell type assignment while processing raw FACS data by gating.

In order to assess how well $\mathcal{M}$ fits the experimental data for a certain set of parameters θ, the log-likelihood $\ell_D(\theta)$ is calculated according to the assumed multiplicative log-normally distributed measurement noise

$$\ell_D(\theta) = -\frac{1}{2} \sum_{s=1}^{n_t} \sum_{n_{div}=1}^{N_{div}} \sum_{j=1}^{|\mathscr{S}|} \log(2\pi\sigma^2_{j,n_{div}}) + \left(\frac{\left(\log(\mathbf{y}^{\mathscr{D}}_{j,n_{div}}(t_s) + 1) - \log(\mathbf{y}^{\mathscr{M}}_{j,n_{div}}(t_s, \theta) + 1) \right)^2}{\sigma^2_{j,n_{div}}} \right). \tag{10}$$

In order to estimate the unknown parameter vector, the optimization problem

$$\theta^{ML} = \underset{\substack{\theta \\ \text{subject to } \mathscr{M}}}{\text{argmax}} \ \ell_D(\theta) \tag{11}$$

is solved using multi-start local hierarchical optimization (Loos et al., 2018) with trust-region-reflective algorithm and $n_{MS} = 1000$ multi starts. With the hierarchical optimization approach $\sigma^2_{j,i_{div}}, j = 1, ..., |\mathcal{S}|, i_{div} = 1, ..., n_{div}$ is analytically calculated each time the log-Likelihood function is evaluated. The noise parameter is therefore not part of the parameter vector. The starting values $(\theta^{start}_i)_{i=1,...,n_{MS}}$ (initial parameter vectors) are determined according to latin hypercube sampling (Eliáš and Vořechovský, 2016; Loos et al., 2018). The resulting optimal parameter is observed at the highest ℓ_D value. To ensure that the optimization procedure converged, we checked if this best log-likelihood value is observed several times for different starting values. The boundaries for parameter values can be found in Table S2. We used the MATLAB toolboxes AMICI (Fröhlich et al., 2017) for model definition and PESTO (Stapor et al., 2018) for parameter inference.

Structural identifiability of candidate models

A model is structurally identifiable if it is possible to determine parameter values from measurements of the model output. A structural identifiability analysis was performed using a method introduced by (Villaverde and Banga, 2017) and the MATLAB toolbox STRIKE-GOLDD (Villaverde et al., 2019; Villaverde and Banga, 2017). This method evaluates the change of the observables along the model dynamics by calculating Lie derivatives. If the change in the Lie derivatives with parameters $\theta_m,\ m = 1, ..., n_\theta$ leads to linear dependent vectors, at least one parameter is structurally non-identifiable. This analysis can thereby reveal which parameters are identifiable and which ones are non-identifiable for the different hierarchies if one assumes ideal noise-free data with a large sample size (Table 3).

Practical identifiability of inferred parameters

To determine the 95% confidence intervals for each parameter and assess the practical identifiability, we calculated the profile likelihood and used it to calculate confidence intervals for the parameters

(Kreutz et al., 2013). We defined a parameter as practically identifiable from a specific sample if its 95% profile-likelihood-based confidence interval is non-overlapping with its lower and upper parameter boundaries (Supplemental Table 2).

Computation time calculation
For every lineage hierarchy and sample, optimization of 1000 multi starts was run in parallel on a machine with two Intel® Xeon® Silver 4214 12-Core (2,2 GHz, 3,2 GHz Turbo, 16,5M L3 Cache) processors (in total 24 workers) and the time for performing parameter inference was tracked.

Model selection
The parameter estimation was performed individually for all individuals and models A-J. We compared and ranked the different models based on their Bayesian Information Criterion (BIC) value. The BIC of model $\mathcal{M}_q(\boldsymbol{\theta})$
is defined as

$$BIC_q := -2\log(P(\mathscr{D}|\theta_q^{ML})) + n_{\theta_q} \cdot \log(n_{obs}), \tag{12}$$

where n_{θ_q} describes the number of parameters of model $\mathcal{M}_q(\boldsymbol{\theta})$ and n_{obs} the number of observations used for model fitting (Neath and Cavanaugh, 2012). The Akaike Information Criterion (AIC, (Akaike, 1992)) of $\mathcal{M}_q(\boldsymbol{\theta})$ is given by

$$AIC_q := -2\ell_{\mathscr{D}}(\theta_q^{\hat{M}L}) + 2n_\theta. \tag{13}$$

Calculation of the AIC or BIC scores provides a ranking of all considered models in which the best performing model is the one with the lowest score

$$\mathscr{M}_{\text{rank 1}} = \mathscr{M}_q, \text{ if } C_q = \min_{m\in\{1,\dots,n_M\}}(C), \tag{14}$$

To derive the set of plausible and implausible models the differences

$$\Delta_j^C := C_j - \min_{m\in\{1,\dots,n_M\}}(C), \tag{15}$$

With C being the AIC or BIC score and j the index of the respective model, are calculated. Model $\mathcal{M}_j$ can be rejected if $\Delta_i^{Score} > 10$ (Guthery et al., 2003). Consequently, for the comparison of two models $\mathcal{M}_1$ and $\mathcal{M}_2$, where $\mathcal{M}_2$ is of higher or equal complexity than $\mathcal{M}_1$ the null hypothesis $\mathcal{H}_0$: "Model $\mathcal{M}_1$ is true." can be rejected if $\Delta^C_{\mathcal{M}_1,\mathcal{M}_2} = C_{\mathcal{M}_1} - C_{\mathcal{M}_2} > 10$. As $\Delta^C_{\mathcal{M}_1,\mathcal{M}_2}$ are given by

$$\begin{aligned}\Delta^{AIC}_{\mathscr{M}_1,\mathscr{M}_2} &= AIC_{\mathscr{M}_1} - AIC_{\mathscr{M}_2} = T(\mathscr{M}_1,\mathscr{M}_2) - 2(n_\theta^{\mathscr{M}_2} - n_\theta^{\mathscr{M}_1})\\ \Delta^{BIC}_{\mathscr{M}_1,\mathscr{M}_2} &= T(\mathscr{M}_1,\mathscr{M}_2) - log(n_{obs})(n_\theta^{\mathscr{M}_2} - n_\theta^{\mathscr{M}_1}),\end{aligned} \tag{16}$$

for AIC and BIC, model $\mathcal{M}_1$ can be rejected if the respective test statistic $T(\mathcal{M}_1,\mathcal{M}_2)$ exceeds critical values of

$$\begin{aligned}v^{AIC}_{crit} &= 10 + 2(n_\theta^{\mathscr{M}_2} - n_\theta^{\mathscr{M}_1}),\\ v^{BIC}_{crit} &= 10 + log(n_{obs})(n_\theta^{\mathscr{M}_2} - n_\theta^{\mathscr{M}_1}).\end{aligned} \tag{17}$$

In silico analysis
To test the implementation, robustness and accuracy of our model selection approach, and if it is able to identify plausible models, we performed an in silico analysis. For each considered lineage hierarchy we implemented the extended model as described in (1) and simulated with a realistic test parameter 3 samples which correspond to the measured differentiation dynamics of 3 individuals which underlie different noise levels. Based on the inference result from fitting experimental data, we defined realistic model-specific test parameters $\theta^{test}_{\mathcal{M}_q}, q = 1,\dots,10$ and simulated data from each model $\mathcal{M}_q \in \{A,B,C,D,E,F,G,H,I,J\}$ with $\theta^{test}_{\mathcal{M}_q}$. We then performed MLE with all models on all in silico data sets and observed which models perform best, are plausible, or can be rejected. Subsequently we fitted each of the 10*3 samples with every considered model and observed if each test parameter lies within the 95% confidence interval of the corresponding optimized parameter, as well as the distance between

test and optimal parameter (Figure S3B), the model fit (Figure S3A, 4A,C) and the BIC scores of each model for each simulated data set for varying noise levels (Figure 4B,D).

Supplemental References

Adolfsson, J., Månsson, R., Buza-Vidas, N., Hultquist, A., Liuba, K., Jensen, C.T., Bryder, D., Yang, L., Borge, O.-J., Thoren, L.A.M., Anderson, K., Sitnicka, E., Sasaki, Y., Sigvardsson, M., Jacobsen, S.E.W., 2005. Identification of Flt3+ lympho-myeloid stem cells lacking erythro-megakaryocytic potential a revised road map for adult blood lineage commitment. Cell 121, 295–306.

Akaike, H., 1992. Information Theory and an Extension of the Maximum Likelihood Principle. Springer Series in Statistics. https://doi.org/10.1007/978-1-4612-0919-5_38

Doulatov, S., Notta, F., Eppert, K., Nguyen, L.T., Ohashi, P.S., Dick, J.E., 2010. Revised map of the human progenitor hierarchy shows the origin of macrophages and dendritic cells in early lymphoid development. Nat. Immunol. 11, 585–593.

Doulatov, S., Notta, F., Laurenti, E., Dick, J.E., 2012. Hematopoiesis: a human perspective. Cell Stem Cell 10, 120–136.

Eliáš, J., Vořechovský, M., 2016. Modification of the Audze–Eglājs criterion to achieve a uniform distribution of sampling points. Advances in Engineering Software. https://doi.org/10.1016/j.advengsoft.2016.07.004

Forsberg, E.C., Serwold, T., Kogan, S., Weissman, I.L., Passegué, E., 2006. New evidence supporting megakaryocyte-erythrocyte potential of flk2/flt3+ multipotent hematopoietic progenitors. Cell 126, 415–426.

Fröhlich, F., Kaltenbacher, B., Theis, F.J., Hasenauer, J., 2017. Scalable Parameter Estimation for Genome-Scale Biochemical Reaction Networks. PLoS Comput. Biol. 13, e1005331.

Galy, A., Travis, M., Cen, D., Chen, B., 1995. Human T, B, natural killer, and dendritic cells arise from a common bone marrow progenitor cell subset. Immunity 3, 459–473.

Giebel, B., Zhang, T., Beckmann, J., Spanholtz, J., Wernet, P., Ho, A.D., Punzel, M., 2006. Primitive human hematopoietic cells give rise to differentially specified daughter cells upon their initial cell division. Blood 107, 2146–2152.

Goardon, N., Marchi, E., Atzberger, A., Quek, L., Schuh, A., Soneji, S., Woll, P., Mead, A., Alford, K.A., Rout, R., Chaudhury, S., Gilkes, A., Knapper, S., Beldjord, K., Begum, S., Rose, S., Geddes, N., Griffiths, M., Standen, G., Sternberg, A., Cavenagh, J., Hunter, H., Bowen, D., Killick, S., Robinson, L., Price, A., Macintyre, E., Virgo, P., Burnett, A., Craddock, C., Enver, T., Jacobsen, S.E.W., Porcher, C., Vyas, P., 2011. Coexistence of LMPP-like and GMP-like leukemia stem cells in acute myeloid leukemia. Cancer Cell 19, 138–152.

Görgens, A., Radtke, S., Möllmann, M., Cross, M., Dürig, J., Horn, P.A., Giebel, B., 2013. Revision of the human hematopoietic tree: granulocyte subtypes derive from distinct hematopoietic lineages. Cell Rep. 3, 1539–1552.

Guthery, F.S., Burnham, K.P., Anderson, D.R., 2003. Model Selection and Multimodel Inference: A Practical Information-Theoretic Approach. The Journal of Wildlife Management. https://doi.org/10.2307/3802723

Hao, Q.L., Zhu, J., Price, M.A., Payne, K.J., Barsky, L.W., Crooks, G.M., 2001. Identification of a novel, human multilymphoid progenitor in cord blood. Blood 97, 3683–3690.

Kreutz, C., Raue, A., Kaschek, D., Timmer, J., 2013. Profile likelihood in systems biology. FEBS J. 280, 2564–2571.

Loos, C., Krause, S., Hasenauer, J., 2018. Hierarchical optimization for the efficient parametrization of ODE models. Bioinformatics 34, 4266–4273.

Majeti, R., Park, C.Y., Weissman, I.L., 2007. Identification of a hierarchy of multipotent hematopoietic progenitors in human cord blood. Cell Stem Cell 1, 635–645.

Månsson, R., Hultquist, A., Luc, S., Yang, L., Anderson, K., Kharazi, S., Al-Hashmi, S., Liuba, K., Thorén, L., Adolfsson, J., Buza-Vidas, N., Qian, H., Soneji, S., Enver, T., Sigvardsson, M., Jacobsen, S.E.W., 2007. Molecular evidence for hierarchical transcriptional lineage priming in fetal and adult stem cells and multipotent progenitors. Immunity 26, 407–419.

Manz, M.G., Miyamoto, T., Akashi, K., Weissman, I.L., 2002. Prospective isolation of human clonogenic common myeloid progenitors. Proc. Natl. Acad. Sci. U. S. A. 99, 11872–11877.

Matis, J.H., Wehrly, T.E., 1990. Generalized stochastic compartmental models with Erlang transit times. J. Pharmacokinet. Biopharm. 18, 589–607.

Neath, A.A., Cavanaugh, J.E., 2012. The Bayesian information criterion: background, derivation, and

applications. Wiley Interdisciplinary Reviews: Computational Statistics. https://doi.org/10.1002/wics.199
Notta, F., Doulatov, S., Laurenti, E., Poeppl, A., Jurisica, I., Dick, J.E., 2011. Isolation of single human hematopoietic stem cells capable of long-term multilineage engraftment. Science 333, 218–221.
Notta, F., Zandi, S., Takayama, N., Dobson, S., Gan, O.I., Wilson, G., Kaufmann, K.B., McLeod, J., Laurenti, E., Dunant, C.F., McPherson, J.D., Stein, L.D., Dror, Y., Dick, J.E., 2016. Distinct routes of lineage development reshape the human blood hierarchy across ontogeny. Science 351, aab2116.
Ostendorf, B.N., Flenner, E., Flörcken, A., Westermann, J., 2018. Phenotypic characterization of aberrant stem and progenitor cell populations in myelodysplastic syndromes. PLoS One 13, e0197823.
Pang, W.W., Price, E.A., Sahoo, D., Beerman, I., Maloney, W.J., Rossi, D.J., Schrier, S.L., Weissman, I.L., 2011. Human bone marrow hematopoietic stem cells are increased in frequency and myeloid-biased with age. Proc. Natl. Acad. Sci. U. S. A. 108, 20012–20017.
Pronk, C.J.H., Rossi, D.J., Månsson, R., Attema, J.L., Norddahl, G.L., Chan, C.K.F., Sigvardsson, M., Weissman, I.L., Bryder, D., 2007. Elucidation of the phenotypic, functional, and molecular topography of a myeloerythroid progenitor cell hierarchy. Cell Stem Cell 1, 428–442.
Reynaud, D., Lefort, N., Manie, E., Coulombel, L., Levy, Y., 2003. In vitro identification of human pro-B cells that give rise to macrophages, natural killer cells, and T cells. Blood 101, 4313–4321.
Rossi, D.J., Jamieson, C.H.M., Weissman, I.L., 2008. Stems cells and the pathways to aging and cancer. Cell 132, 681–696.
Sanjuan-Pla, A., Macaulay, I.C., Jensen, C.T., Woll, P.S., Luis, T.C., Mead, A., Moore, S., Carella, C., Matsuoka, S., Bouriez Jones, T., Chowdhury, O., Stenson, L., Lutteropp, M., Green, J.C.A., Facchini, R., Boukarabila, H., Grover, A., Gambardella, A., Thongjuea, S., Carrelha, J., Tarrant, P., Atkinson, D., Clark, S.-A., Nerlov, C., Jacobsen, S.E.W., 2013. Platelet-biased stem cells reside at the apex of the haematopoietic stem-cell hierarchy. Nature 502, 232–236.
Stapor, P., Weindl, D., Ballnus, B., Hug, S., Loos, C., Fiedler, A., Krause, S., Hroß, S., Fröhlich, F., Hasenauer, J., Wren, J., 2018. PESTO: Parameter EStimation TOolbox. Bioinformatics 34, 705–707.
Takano, H., Ema, H., Sudo, K., Nakauchi, H., 2004. Asymmetric division and lineage commitment at the level of hematopoietic stem cells: inference from differentiation in daughter cell and granddaughter cell pairs. J. Exp. Med. 199, 295–302.
Villaverde, A.F., Banga, J.R., 2017. Dynamical compensation and structural identifiability of biological models: Analysis, implications, and reconciliation. PLoS Comput. Biol. 13, e1005878.
Villaverde, A.F., Evans, N.D., Chappell, M.J., Banga, J.R., 2019. Input-Dependent Structural Identifiability of Nonlinear Systems. IEEE Control Syst. Lett. 3, 272–277.